The Hydrological Impact of Geoengineering in the Geoengineering Model Intercomparison Project (GeoMIP)

Simone Tilmes,[1] John Fasullo,[1] Jean-Francois Lamarque,[1] Daniel R. Marsh,[1] Michael Mills,[1] Kari Alterskjær,[2] Olivier Boucher,[3] Jason N. S. Cole,[4] Charles L. Curry,[5] Jim Haywood,[6,7] Peter J. Irvine,[8] Duoying Ji,[9] Andy Jones,[6] Diana B. Karam,[10] Ben Kravitz,[11] Jón E. Kristjánsson,[2] John Moore,[9] Helene Muri,[2] Ulrike Niemeier,[12] Philip J. Rasch,[11] Alan Robock,[13] Hauke Schmidt,[12] Michael Schulz,[3] Yang Shuting,[14] Balwinder Singh,[11] Shingo Watanabe,[15] and Jin-Ho Yoon[11]

[1] National Center of Atmospheric Research, Boulder, Colorado, USA

[2] Department of Geosciences, Meteorology and Oceanography Section, University of Oslo, Oslo, Norway

[3] Laboratoire de Météorologie Dynamique, IPSL, CNRS/UPMC, Paris, France

[4] Canadian Centre for Climate Modeling and Analysis, Environment Canada, Toronto, ON

[5] School of Earth and Ocean Sciences, University of Victoria, Victoria, BC

[6] Met Office Hadley Centre, Exeter, UK

[7] Exeter Climate Systems, University of Exeter, Exeter, UK

[8] Institute for Advanced Sustainability Studies, Potsdam, Germany

[9] State Key Laboratory of Earth Surface Processes and Resource Ecology, College of Global Change and Earth System Science, Beijing Normal University, Beijing, China

[10] Laboratoire des Sciences du Climat et l'Environnement, CEA, CNRS, UVSQ, Gif-sur-Yvette, France

[11] Pacific Northwest National Laboratory, Richland, WA

[12] Max Planck Institute for Meteorology, Hamburg, Germany

[13] Department of Environmental Sciences, Rutgers University, New Brunswick, NJ

[14] Danish Meteorological Institute (DMI)

[15] Japan Agency for Marine-Earth Science and Technology, Yokohama, Japan

Simone Tilmes (e-mail: tilmes@ucar.edu).

Abstract. The hydrological impact of enhancing Earth's albedo by solar radiation management is investigated using simulations from 12 models contributing to the Geoengineering Model Intercomparison Project (GeoMIP). We contrast an idealized experiment, G1, where the global mean radiative forcing is kept at pre-industrial conditions by reducing insolation while the CO_2 concentration is quadrupled, to a 4xCO_2 experiment. Global average temperature in G1 is preserved at its pre-industrial value, but precipitation is reduced by around 4.4% compared to the control, while it is increased by around 6.2% in the 4xCO_2 experiment. An initial reduction of evapotranspiration over land with instantaneously increasing CO_2 concentrations in both experiments largely contributes to a reduction in evaporation. A warming surface associated with the transient adjustment in 4xCO_2 generates an increase of global precipitation, with considerable regional changes, such as a drastic precipitation increase of 10% over India and East Asia but also a reduction of 7% for the North American summer monsoon. Reduced global evaporation (10%) and precipitation persists in G1 with precipitation reduction over monsoonal land regions: East Asia (6%), South Africa (5%), North America (7%) and South America (6%). Uncertainties of results are discussed. In contrast to the 4xCO_2 experiment, where the frequency of months with heavy precipitation intensity is increased by over 50% in comparison to the control, a reduction of up to 20% is simulated in G1. These changes in precipitation in both total amount and frequency of extremes, point to a considerable weakening of the hydrological cycle in a geoengineered world.

1. Introduction

Geoengineering, also called climate engineering, is discussed in recent literature as a potential option for reducing the most dangerous changes to Earth's climate as a result of large greenhouse gas increases [*Launder and Thompson*, 2009]. One of the proposals to "buy some time" while mitigation scenarios are aggressively ramped up, considers the reduction of incoming shortwave radiation, called Solar Radiation Management (SRM). This approach is expected to offset the warming arising from increasing greenhouse gas concentrations with a corresponding reduction in solar absorption [e.g., *Crutzen*, 2006].

Natural analogues for SRM have been observed after the occurrence of large volcanic eruptions, such as that of Mt. Pinatubo in 1991, which injected 20 Mt of SO_2 into the stratosphere [*Bluth et al.*, 1992]. The increased planetary albedo arising from stratospheric volcanic aerosols resulted in a temporary cooling of the Earth's surface of about 0.5 K [*Soden et al.*, 2002]. However ancillary effects were also observed, such as a weakening of the hydrological cycle, which was identified based on a significant reduction of the continental river discharge [*Trenberth and Dai*, 2007]. Further, an increase in stratospheric ozone depletion in the Arctic polar vortex was observed in the two years following the eruption [*Tilmes et al.*, 2008]. Simulations of a geoengineered atmosphere using sulfate aerosols also indicate changes in stratospheric dynamics and chemistry caused by SRM [*Tilmes et al.*, 2009; *Heckendorn et al.*, 2009].

Increasing greenhouse gas concentrations are heating the planet and warming the surface and troposphere, leading for instance to increases in atmospheric water vapor [*Solomon et al.*, 2007]. Combined with an increased net downward radiative flux, these transient feedbacks result in a strengthening of the hydrological cycle, characterized by an increase in both total rainfall and

the frequency of heavy precipitation events [*Trenberth*, 1999; *Trenberth et al.*, 2003; *Held and Soden*, 2006; *Solomon et al.*, 2007]. Furthermore, a robust contrast of hydrologic and radiative feedbacks between land and ocean is observed [e.g., *Wang and Ding*, 2006; *Sutton et al.*, 2007] and simulated by climate models in a high CO_2 environment [e.g., *Joshi et al.*, 2008; *Fasullo*, 2010, 2012; *Lambert et al.*, 2011]. Greater warming over land than over the ocean leads to contrasting feedbacks with reductions in low level relative humidity over land increasing the lifting condensation level and suppressing rainfall increases relative to those over ocean.

SRM has been suggested as a mechanism to stabilize global temperatures. The continuous increase in positive forcing from increasing greenhouse gases is countered by a continuous increase in negative forcing from SRM produced by an increase in the Earth's albedo. This may be achieved by adjusting the amount of aerosol loading in the stratosphere [e.g., *Wigley*, 2006]. However, such experiments will alter the flow of energy throughout the climate system and reduce surface downwelling shortwave and latent heat fluxes, as studied in many different model scenarios [*Govindasamy and Caldeira*, 2000; *Govindasamy et al.*, 2003; *Lunt et al.*, 2008; *Bala et al.*, 2008; *Hegerl and Solomon*, 2010; *Irvine et al.*, 2010; *Schmidt et al.*, 2012; *Pongratz et al.*, 2012]. Some geoengineering studies have shown a significant decrease of precipitation, for example, over the Indian monsoon, as a result of geoengineering [*Robock et al.*, 2008; *Jones et al.*, 2010]. *Kravitz and Robock* [2011] and *Haywood et al.* [2013] have explored scenarios where injections of aerosol were made into solely one hemisphere, which results in different regional precipitation responses. However, different models and scenarios do not always agree in the sign of the change of monsoonal precipitation in response to geoengineering [*Rasch et al.*, 2008; *Jones et al.*, 2010]. Therefore, the impact of SRM in the context of a high CO_2

environment on the global and regional precipitation across different climate models has yet to be quantified.

To explore the impact of geoengineering on the climate system, the Geoengineering Model Intercomparison Project (GeoMIP) was initiated [*Kravitz et al.,* 2011]. A set of geoengineering experiments was designed in conjunction with the fifth phase of the Coupled Model Intercomparison Project (CMIP5) effort [*Taylor et al.,* 2012]. These geoengineering experiments were performed by a number of modeling groups. Here, we use the experiment called "G1" in which the incoming solar radiation at the top of the atmosphere (TOA) is reduced to balance the radiative forcing at the TOA in an atmosphere with four times the pre-industrial CO_2 concentration (4xCO_2). This experiment thus depicts a strongly forced case of geoengineering with carbon dioxide concentrations at 1139 ppm, providing a robust signal-to-noise ratio relative to internal variability. This forcing is roughly equivalent to the RCP8.5 radiative forcing by the end of the 21st century.

A detailed investigation of global and regional precipitation and evaporation changes in two experiments is performed: 1) an abrupt 4xCO_2 increase and 2) G1, compared to 1850 control conditions, is discussed in this paper, with a particular focus on changes over monsoonal regions. The following questions are addressed: Do climate models simulate a robust response of SRM in global and regional precipitation and how does the magnitude compare to the 4xCO_2 response? How does SRM impact precipitation intensities globally and in different regions? And finally, what is the relative compensation for CO_2-induced changes and are there distinct differences evident from SRM, over land and ocean?

We quantify the global and regional hydrologic changes based on GeoMIP model simulations, which are summarized in Section 2. The global temperature and precipitation response to

112 CO_2 quadrupling and SRM for individual models are discussed in Section 3. In Section 4, we
113 investigate the question of how much SRM in a high CO_2 environment changes global and re-
114 gional precipitation patterns in comparison to 1850 conditions. We contrast these results to the
115 4xCO_2 experiment without SRM and focus on large-scale features in the tropics and northern
116 mid-latitudes. Beyond analyzing the response of total precipitation and evaporation, changes
117 in the frequency of various precipitation intensities are also assessed, providing further insight
118 into the changing character of rainfall. Section 5 focuses on monsoonal regions, as defined by
119 *Wang and Ding* [2006], who provide an objective method for comparison of monsoon variabil-
120 ity among observations and models. The separation of monsoonal land and ocean components
121 helps to isolate contrasting responses based on constraints imposed by surface albedo and mois-
122 ture effects. The ability of models to reproduce the area of observed monsoonal regions and
123 precipitation amounts is evaluated in Section 5.1 and the hydrologic changes in both 4xCO_2
124 and G1 relative to pre-industrial conditions are investigated in Section 5.2. In Section 6, we
125 discuss results in the context of the hydrological cycle and a summary is given in Section 7.

2. Model Experiments and Analysis

126 Results from 12 climate models are used that each performed three model experiments: a
127 preindustrial control (labeled 1850), an abrupt quadrupling of CO_2 (labeled 4xCO_2), and the
128 G1 GeoMIP experiment that adds SRM to the 4xCO_2 scenario. A detailed description of the
129 setup of the GeoMIP experiments is outlined in *Kravitz et al.* [2011]. For each experiment, up to
130 three ensemble members are available per model. The 1850 control simulations are derived from
131 an extended integration designed to produce equilibrated global-mean surface temperatures. At
132 least 50 years of this well-balanced experiment are available for all models.

The 4xCO_2 experiment (also called "abrupt4xCO_2") is started from the 1850 control experiment and the simulation extended for 150 years for most models (2 models provided only 50 and 75 year simulations) (Table 1, second column). For this simulation a strong radiative imbalance exists for at least 10 years at the TOA caused by a CO_2 forcing of about 6 to 9 Wm^{-2} [*Kravitz et al.*, 2013]. For this reason, precipitation and temperature changes from the first 10 years of this experiment are not considered. However, all subsequent years of the 4xCO_2 experiment are included in our analysis in order to maximize the number of years per simulation for all the models, including those with shorter simulations. Since the 4xCO_2 simulations still experience moderate transient adjustment after the first decade, considering 10 – 150 years for most of the models results in a slightly smaller ($\approx$ 0.5 K) average temperature change and $\approx$ 0.5% smaller precipitation change compared to the results presented in Table 4 by *Schmidt et al.* [2012], who considered the years 101 to 150.

The G1 experiment is branched off the 1850 control experiment. The climate in this experiment is controlled by two forcings, an instantaneous quadrupling of CO_2 and a corresponding reduction of incoming solar radiation in reduction the solar constant to balance the residual TOA imbalance. The experiment is performed for 50 years with 1 to 3 ensemble simulations [*Kravitz et al.*, 2013]. We include all available years of the G1 simulation in our analysis (Table 1, third column), following the approach of *Schmidt et al.* [2012]. The simulation is designed to portray a strongly forced climate system, to produce a large signal-to-noise ratio in the context of internal variability in response to solar dimming. These results are expected to differ to some degree from transient geoengineering experiments, which are characterized by a steady ramp-up of greenhouse gas concentrations and solar dimming. However, many of the principal processes are expected to be similar between the two simulations, as further discussed below.

General features of the climate response in the G1 experiment are described by *Kravitz et al.* [2013] and by *Schmidt et al.* [2012] who considered only a subset of the models. For the G1 simulation, the incoming shortwave radiation was reduced by an amount that differed a bit between individual model, ranging from 3.8% to 5.0% (Table 1, last column). This value differs across models due to their individual responses to solar dimming, for instance due to differences in cloud feedbacks [*Schmidt et al.*, 2012]. Most models were able to achieve a global balance. However, as described by *Schmidt et al.* [2012] and *Kravitz et al.* [2013], spatial and temporal structure in net radiative forcing at TOA ($\mathrm{F_{TOA}}$) persists due to differences in spatiotemporal patterns of the two opposing forcings, resulting in a net decrease of the $\mathrm{F_{TOA}}$ at low latitudes, and a net increase in high latitudes. Consequently, a cooling in comparison to 1850 conditions was found in the tropics, while the high latitudes warm strongly with a maximum in winter for each hemisphere. Precipitation changes were briefly investigated in these studies, considering the change of global mean precipitation, changes in the Bowen ratio [*Schmidt et al.*, 2012], and the difference between precipitation and evaporation [*Kravitz et al.*, 2013]. Based on results from only four models, *Schmidt et al.* [2012] identified a consistent decrease of precipitation in South-East Asia for all the models, while models do not agree in sign for the other monsoonal regions. *Kravitz et al.* [2013] found a reduction in precipitation minus evaporation ($P - E$) by up to 1.4 mm day^{-1} in some tropical regions but less than 0.2 mm day^{-1} in summer over monsoonal regions for the ensemble mean.

In our analysis we contrast precipitation and evaporation changes of two perturbed experiments, the 4x$\mathrm{CO_2}$ and the G1 experiment, in comparison to 1850 control conditions. Monthly outputs for near surface temperature, total precipitation and evaporation are used from available ensemble members provided by each model group. Area-weighted global and regional

responses are derived. Other variables such as runoff and soil moisture that are part of the hydrological cycle vary greatly between models, and there are uncertainties in observations of the fields, so we choose not focus on them in this study (see Section 6 for further discussion).

Specifics of each model, including their vertical and horizontal resolution and climate sensitivity, are summarized by *Kravitz et al.* [2013] (suppl. online material, Table S1). Model parameterizations of convection and microphysics are listed in Table 2.

3. Global Temperature and Precipitation Response

The simulated global surface air temperature response in the 4xCO_2 experiment compared to the 1850 control experiment varies in proportion to model sensitivity [*Gregory et al.*, 2004]. The global average temperature change from model to model differs by 2.9 K to 5.9 K, ignoring the first 10 years of the simulation (Figure 1, top panel, and Table 1, fourth column). Changes in global precipitation between the 4xCO_2 and the control experiment are positively correlated to warming and, therefore, to climate sensitivity. The increase of global precipitation derived from different models ranges between 45 and 110 mm a^{-1} (4.5 – 12%) with the GISS model being an outlier showing an increase of only about 20 mm a^{-1} or 2%.

The initial decrease of precipitation due to the instant quadrupling of CO_2 in the first few months of the simulation is called the "fast response" or "rapid adjustment" [e.g., *Andrews et al.*, 2009; *Andrews and Forster*, 2010], and is followed by the transient feedback, usually called the "slow response". The fast response is believed to be caused by the initial increase of atmospheric stability in a high CO_2 environment. The transient feedback is driven by changes in surface temperature, which is a function of the uptake of heat by the ocean in a warming climate and its impact on water vapor and the divergent tropical circulation [e.g., *Held and*

Soden, 2006]. Precipitation changes in models are often reported in changes per K considering the slow response only.

The transient feedback is estimated here by fitting a straight line through the annual averaged global precipitation changes versus temperature changes for the first 10 years of the 4xCO_2 experiment started from 1850 average conditions (Figure 1, thin colored line). Intersections of each line with the x-axis can be understood as the fast response of the precipitation for each model for the 4xCO_2 experiment (see *Andrews et al.* [2009]).

The estimated range of the transient feedback is 20 – 35 mm a^{-1} K^{-1} (2.0 - 3.5% K^{-1}), which is less than what would be expected from the increase in water vapor ($\approx$ 7% K^{-1}) due to a weakened divergent circulation. GeoMIP and therefore CMIP5 results are in good agreement with earlier studies using the CMIP3 archive (*Held and Soden* [2006], 2.2% K^{-1}, *Andrews and Forster* [2010], 2.4% K^{-1}). The transient feedback will not be further discussed, since it does not include the transient adjustment of the fast response, and therefore results in an overestimation of the precipitation response to a CO_2 increase [*Andrews and Forster*, 2010].

Contrasting G1 and 4xCO_2 simulations highlights the precipitation response to solar dimming in a high CO_2 environment (Figure 1, lower left quadrant of each panel). Global mean temperatures in the G1 experiment are 3.2 – 6.1 K cooler compared to the 4xCO_2 experiment (Figure 1, top panel; Table 1, fifth column) and precipitation rates are reduced by 90 to 140 mm a^{-1} (8 – 12.5%) for most models, with the largest reduction of 170 mm a^{-1} (16%) in IPSL-CM5A-LR. Precipitation changes due to decreases in solar forcing are largely governed by the slow response referred to above [*Andrews and Forster*, 2010]. These changes are very similar, but have opposite sign compared to the slow response under the transient adjustment of the 4xCO_2 experiment, as they relate to changes in the surface energy balance. Global mean

precipitation differences between G1 and 4xCO_2 are also positively correlated to the surface temperature change (correlation coefficient $r = 0.80$).

On the other hand, considering the G1 experiment with regard to 1850 conditions, global mean surface temperatures do not change significantly (Figure 1, middle cluster). Global precipitation decreases by 47 $\pm$ 15 mm a^{-1} (4.5 $\pm$ 1.3%) (see Figure 1). Global average precipitation deviations from the control are thus more than half of the precipitation changes induced by a quadrupling of CO_2. Total precipitation amount is controlled by the surface energy budget [*Hansen et al.*, 1997] and the slow response in the precipitation rate is expected to be small. All the models simulate a global near-surface temperature change within $\pm$ 0.3 K compared to the control, whereas the BNU-ESM model is biased high by 0.63 K (Table 1, column 6). Interestingly, the precipitation reduction in G1 is correlated to the fast response of the 4xCO_2 experiment ($r = 0.88$, if ignoring the BNU-ESM model) with a slightly smaller reduction in precipitation than suggested by the fast response (Figure 2). Therefore, models with the largest fast response of the 4xCO_2 experiment also produce the greatest reductions in precipitation in response to solar dimming.

This suggests that both the fast response in the 4xCO_2 experiment and the hydrologic sensitivity under G1 forcing may underlay a similar mechanism. An initial increase in atmospheric stability in the G1 experiment is shown by *Kravitz et al.* [2013] and is also simulated for other geoengineering experiments [e.g., *Bala et al.*, 2008]. However, *Fyfe et al.* [2013] and *Schmidt et al.* [2012] have suggested that the reduction in evapotranspiration from plants over land [e.g., *Doutriaux-Boucher et al.*, 2009; *Cao et al.*, 2010] plays an important role as well. In Appendix A, we explore this issue using the NCAR CCSM4 in contrasting results of the first year of the model experiments performed with and without an interactive land carbon cycle. We show that

the abrupt CO_2 increase reduces the stomatal conductance and results in a similar initial change of surface fluxes in both the 4xCO_2 and G1 experiments. For the first year of the simulation, reduced evapotranspiration is responsible for the reduction of upwelling latent heat flux over land with consequences for precipitation and surface temperatures, but with little change over the ocean.

The reduction in precipitation for G1 experiments is therefore largely influenced by CO_2 concentration changes. This is discussed by *Fyfe et al.* [2013]. Models that do not include the interactive land carbon cycle, and therefore do not consider stomatal conductance, simulate smaller reductions in precipitation than those that include this process. These findings are also in agreement with the GeoMIP results, showing the smallest precipitation response to CO_2 for the EC-EARTH DMI, the only model that does not include this process. If the evapotranspiration from plants scale inversely with CO_2 concentration, we also expect precipitation in transient SRM model experiments to vary inversely with CO_2. Nevertheless, changes in surface temperature are the most important factor that control changes in maximum precipitation events on the large scale, as was already found in CO_2 ramp-up and down experiment by *Boucher et al.* [2012].

Therefore, even though global surface temperatures do not generally change in G1 compared to 1850 conditions, precipitation changes are a likely result of both the influences of changes in atmospheric stability and stomatal conductance over land. Since we do not find a correlation between precipitation reduction in the G1 experiment and climate sensitivity, we report absolute precipitation and evaporation changes for the 4xCO_2 and the G1 experiments rather than those normalized by temperature changes (see *Bala et al.* [2008]).

4. Precipitation and Evaporation Response in Tropics and Mid-Latitudes

Zonal mean precipitation and evaporation responses in the 4xCO_2 and G1 experiments are derived for land and ocean separately (Figure 3). In the remainder of the text, model responses are always shown in comparison to 1850 conditions. Precipitation decreases in G1 over both land and ocean, with similar latitudinal structure. The strongest reduction occurs in the tropics and northern mid-latitudes (as further discussed below). Changes in the 4xCO_2 experiment are relatively large and exhibit distinct latitudinal structure between land and ocean. Further, evaporation is significantly smaller over land compared to the ocean for both the G1 and 4xCO_2 experiment. For G1, evaporation decreases by around 10% over land, while changes over the ocean are small.

With an intensification of the hydrologic cycle in 4xCO_2 conditions, rainfall and evaporation increase generally, with reductions in the subtropics over ocean [e.g., *Durack et al.*, 2012]. The reduction of precipitation in the 25°S – 45°S latitude band over the ocean coincides with a strong decrease in cloud amount and relative humidity [*Fasullo and Trenberth*, 2012] and is also connected to poleward shifts in the mid-latitude storm tracks [*Scheff and Frierson*, 2012]. The disproportionate reduction in evaporation over land compared to the ocean is due to the reduced stomatal conductance of plants in a high CO_2 environment, as discussed in Appendix A.

In the following, we distinguish between global and regional responses of each experiment, including monsoon components, the Intertropical Convergence Zone (ITCZ) and the mid-latitudes. Monsoon components, as shown in Figure 4, are derived using the criteria of *Wang and Ding* [2006]. These criteria are based on the local annual range (AR) of precipitation, which is defined as the difference between total summer (JJA for the Northern Hemisphere, DJF for

the Southern Hemisphere) and winter (DJF for the Northern Hemisphere, JJA for the Southern Hemisphere) precipitation. Regions are defined to be monsoonal if the AR exceeds 180 mm and the local summer monsoon precipitation comprises at least 35% of the total annual rainfall [*Wang and Ding*, 2006]. In addition to the regions identified by *Wang and Ding* [2006], we consider two sub-regions of Asia: India and East Asia. These criteria are applied to the GeoMIP simulations and to two independent precipitation datasets (as discussed in Section 5.1). The global mean intensity of the summer monsoon preciption of all identified monsoon components is defined as the global monsoon index (GMI) [*Wang and Ding*, 2006]. The ITCZ is defined here as the region between 25°N and 25°S, excluding any monsoonal regions in this latitude band, to distinguish between their respective precipitation responses. We report mean and median values of multi-model results and consider changes to be robust if 75% of all models agree on the sign of the change. Further, the mean interannual variability of the experiment has to be smaller than the change compared to the control to produce a significant result.

We also assess relative changes in frequency of precipitation intensities based on monthly averaged values, as demonstrated in Figure 5. The shape of the precipitation distribution is obviously not Gaussian and its statistics can be more precisely expressed in terms of percentiles rather than in the mean of the distribution (Figure 5, lower part). Consideration of changes in the probability density functions (PDFs) helps to identify, for instance, changes in the tail of the distribution, similar to the method of *O'Gorman* [2012]. For the global average, the 4xCO_2 simulations have significantly more frequent occurrences of large monthly mean precipitation events than the control simulations; the G1 experiments are much closer to the control for the 99th percentile and SRM has generally a reduced probability of extreme precipitation events. A

detailed assessment of changes in extreme precipitation events, drizzle and storms, on a daily basis is beyond the scope of this work and will be performed in future studies.

4.1. Large Scale Features and Tropical Response

For the 4xCO_2 experiment, the global multi-model mean (MMM) precipitation over land is 34 mm a^{-1} (3.6%) larger compared to the control (Table 3, third column), with an agreement in sign for less than 75% of the models, as indicated by the quartiles in Figure 6 (top and middle panels). Three models show a decrease of precipitation over land in the 4xCO_2 experiment (see Table 3). The GISS model simulates the largest global reduction over land, aligned with the largest fast response (as discussed above) and a stronger reduction in evaporation over land compared to the other models. Over the ocean, models show a robust increase of 79 mm a^{-1} (6.8%) compared to the control simulation (Figure 6, top and middle panel). In contrast, precipitation for the G1 experiment decreases robustly by 43 mm a^{-1} (4.5%) over land and 50 mm a^{-1} (4.3%) over the ocean (Table 3, fourth column). The multi-model median global precipitation changes (Figure 6, dark red and grey squares) are different from the MMM values, because outliers are valued less in this measure. Multi-model median precipitation changes over land and ocean in the 4xCO_2 are more similar to each other than considering the MMM, with values of around 6.2%. For G1, the multi-model median precipitation reduction is 3.6% over land and 4.6% over the ocean. Therefore, MMM precipitation reduction over land for both experiments is amplified by the outliers. For regional changes, we only report multi-model median precipitation changes.

A large portion of global precipitation occurs over the monsoonal regions and ITCZ (Figure 6, top and middle panel). An increase in precipitation is simulated in 4xCO_2 in both monsoonal land and ocean regions of 68 mm a^{-1} (5.2%) and 118 mm a^{-1} (8.1%), respectively, and in oceanic ITCZ regions of 80 mm a^{-1} (5.3%). This increase is qualitatively consistent with what

was found in the CMIP3 archive by *Fasullo* [2012] and the CMIP5 archive [*Hsu et al.*, 2013; *Lee and Wang*, 2012]. In the land ITCZ region, the multi-model median precipitation increased by 58 mm a^{-1} (6.9%), however, the sign of projected precipitation changes is not consistent among models. The limit extent of the land monsoon region and its associated susceptibility to internal variability of this region might cause these inconsistencies.

In contrast, the G1 simulations show a robust decrease in monsoonal precipitation of 56 mm a^{-1} (4.2%) over land and 66 mm a^{-1} (4.5%) over the ocean (Figure 6, top, and middle panel). Precipitation in the ITCZ is reduced by around 5% with a larger interannual variability and spread among the models over land compared to the ocean. Deviation from preindustrial values is slightly smaller in G1 than for the 4xCO_2 simulations.

For the 4xCO_2 experiment, evaporation increases globally, particularly in the tropics over the ocean between 6 and 10% while it does not significantly change over land (Figure 6, bottom left panels), in agreement with earlier work [*Held and Soden*, 2006; *Seager et al.*, 2010]. These studies show reductions in $P-E$ over the ocean and increases over land in the tropics take place in a warming climate. For the G1 experiment, evaporation decreases monotonically over both land and ocean, with a significantly stronger decrease over land consistently for all the models with values around 10% over land and 4% over the ocean (Figure 6, bottom right panel).

Along with the increase in precipitation for the 4xCO_2 experiment, precipitation intensity frequencies for months with small to medium intensities precipitation (below 8 mm day^{-1}) in the monsoon domains and ITCZ are reduced by 10% and 20%, respectively (Figure 7, left panels). This reduction in the 4xCO_2 experiment is qualitatively consistent with a decrease in relative humidity in the lower troposphere, a higher lifted condensation level, and increased convective inhibition in a warming climate [e.g., *Hansen et al.*, 1997; *Fasullo*, 2010]. On the

other hand, we find a significant increase in the intensity of frequency of heavy precipitation (99th percentile of the PDF) reaching values of above 80% for the monsoon and around 50% for ITCZ (Figure 7, left). This is consistent with estimations by *O'Gorman* [2012], following the concept of "rich get richer" referring to wet regions getting wetter and dry regions getting drier [*Kharin et al.*, 2007; *Sun et al.*, 2007; *Neelin et al.*, 2009; *O'Gorman and Schneider*, 2009; *Chou et al.*, 2009; *Xie et al.*, 2010].

The relative changes in precipitation frequencies for monsoonal regions in G1 (Figure 7, right) indicate that the frequency of intense global precipitation is more strongly reduced over land than over the ocean, even though the PDF for the ocean describes a longer tail than for the land. Heavy monsoon rainfall ($>$ 10 mm day^{-1}) over land is reduced in frequency by around 20% (further discussed in Section 5.2). A considerable reduction in frequency of heavy precipitation ($>$ 8 mm day^{-1}) over the ITCZ is found for both land and ocean with values up to 20% for land and up to 30% for the ocean for the 99th percentile of the PDF. This reduction in the frequency of precipitation accompanies a pronounced reduction in evaporation. In comparison to the 4xCO_2 simulations, perturbations from preindustrial intensities of heavy precipitation are much smaller in G1.

4.2. Seasonal Precipitation Response in Mid-Latitudes

Precipitation in mid- and high latitudes is influenced by both local temperature and relative humidity changes and by the moisture transport from low to mid-latitudes [*Trenberth et al.*, 2003], which vary with season. The strong warming toward higher latitudes in the 4xCO_2 experiment results in increased evaporation and precipitation (as discussed above). In the 45°N – 65°N latitude band for the 4xCO_2 experiment, a disproportionate increase in frequency of medium intensity precipitation is found over land compared to the ocean in winter (see Fig-

ure 8), in alignment with a stronger warming over land than over the ocean (colored diamonds in Figure 8). In addition, heavy precipitation frequencies increase more strongly over the ocean compared to the land (Figure 8, left). In contrast, the frequency of summer median precipitation of 1 – 3 mm day^{-1} is reduced for both land and ocean while the frequency of months with heavy precipitation intensities rises above 50% for the 95th percentile of the PDF. These changes likely result in increased aridity in the region, as higher frequencies of heavy rainfall are generally associated with increased runoff [*Trenberth and Dai*, 2007].

The response of precipitation and evaporation in G1 is robust and negative for all latitude zones except for southern latitudes of 65°S – 90°S (not shown). The strongest relative reduction outside the tropics occurs between 45°N – 65°N, with a decrease in precipitation of 6% over land and 4% over the ocean (Figure 3, right). Seasonal changes are much more pronounced than annual average values (not shown). In summer, a robust reduction of precipitation frequency of around 30% over land and around 25% over the ocean is simulated for months with precipitation intensities between 3 and 7 mm day^{-1}. This reduction occurs even though temperatures are about half a degree warmer in mid-latitudes over land for this season. On the other hand precipitation changes are rather small in winter. The strong reduction of the frequency of medium and heavier precipitation (Figure 8, right) at 45°N – 65°N over land coincides with a suppression of clouds, as pointed out by *Schmidt et al.* [2012].

5. Monsoonal Regions

5.1. Evaluation of Precipitation in Monsoonal Regions

Detailed evaluation of the representation of the global monsoon for a more complete set of CMIP5 models is given in *Hsu et al.* [2013]; *Lee and Wang* [2012] and *Sperber et al.* [2012]. Here, we focus on evaluating the simulated monsoon areas (shown in Figure 4) and seasonal-

ity of precipitation in GeoMIP models using two precipitation datasets, the Global Precipitation Climatology Project (GPCP) and the Tropical Rainfall Measuring Mission (TRMM) [*Liu et al.*, 2012]. The GPCP dataset is based on merged multispectral satellite retrievals and surface observations between 1979 and 2010 [*Adler et al.*, 2003]. TRMM precipitation estimates are derived from merging satellite radar retrievals with surface gauge estimates [*Huffman et al.*, 2009]. While the TRMM estimates are not global, they do cover latitudes of the major monsoon systems. Both datasets have shortcomings related to their ability to detect shallow and extratropical rainfall, and distinguish between suspended and falling hydrometeors. Recent work has suggested that as a result, these products systematically underestimate rainfall amounts [*Stephens et al.*, 2012], though it remains a challenge to balance the surface energy budget under these assumptions. Consistent with this, models simulate larger rainfall amounts than the retrieval estimates by an average of 0.3 mm day^{-1}, or 12% (see Table 3, second column), however much of this excess rainfall is associated with known biases in their representation of the ITCZ [e.g., *Lin*, 2007; *Zheng et al.*, 2012]. As such, resolving these issues lies beyond the scope of this manuscript and the range of observations will be estimated here using GPCP and TRMM datasets. Even though the period of observed precipitation does not coincide with the experiments performed, evaluation of its large-scale features is possible since changes across the experiments are in general less than the differences between the two observational datasets (see Figure 9).

The MMM area of the global-land monsoon for all three experiments is similar to that observed, but the global-ocean monsoon area is smaller for most models (Figure 9). The monsoon domain was shown to not change appreciably over land with increasing CO_2 concentrations, besides some changes over Asia were identified [*Lee and Wang*, 2012], which are not apparent

using the GeoMIP models. The largest model spread of the land monsoon extent occurs in East Asia and Australia. The area of the West African land monsoon component is smaller than observed in all models. Over the ocean, the simulated monsoon areas vary more widely across models than over land and simulated ocean monsoonal regions are generally smaller than observed in Australia, South Africa, and the South Pacific Convection Zone (SPCZ) while they are larger than observed in South America. For these regions it is known that model biases are characterized by an excessive Pacific cold tongue and Atlantic zonal gradient. Under G1 forcing, the area of the monsoonal regions decreases over both land and ocean, generally, while for 4xCO_2 conditions, increases in extent are simulated over ocean. The observed land-to-ocean ratio of global precipitation of 0.89 (for GPCP) is on average 7% smaller in models and falls below 0.80 in half of the models in the GeoMIP archive, resulting in a MMM of 0.82 (Table 4). For the 4xCO_2 experiment, the models show on average a slight reduction in the land to ocean ratio, suggesting a stronger increase of precipitation over the ocean than over land due to moisture constraints over land and additional warming [e.g., *Fasullo*, 2012]. In the G1 experiments, the land to ocean ratio in the MMM does not change significantly and individual models simulate differences in comparison to observations ranging between -6% to and 3%.

The seasonal cycle of global monsoon precipitation over land for 1850 control conditions is compared to the two independent precipitation datasets (Figures 10 and 11). The comparison is valid since precipitation changes between 1850 and present day are not expected to be larger than the estimated transient feedback (2 – 3% K^{-1}), which is less than the uncertainty of observations. Model precipitation over land is in general larger than observed in the summer SH monsoons (Figure10). Biases and inter-model spread in monthly mean summer precipitation are greater over ocean monsoonal regions, than over land, and are particularly large for the

SPCZ (Figure11). Summer precipitation is larger than reported in observations for the MMM in most regions. The seasonal cycle of the Indian monsoon over ocean has its onset in May and maximum in June, which is delayed in most models, in agreement with findings by *Seth et al.* [2010] and *Sperber et al.* [2012].

The MMM (Figures 10 and 11) and the mean interannual variability of precipitation over monsoonal regions for 1850 control conditions is for most regions within the range of GPCP and TRMM, even though there are large differences between individual models. Simulated deficiencies occur for the Australian, North and South American and South African land monsoon components and for the South American and SPCZ ocean monsoon. The simulated variability is excessive for the Indian and South African oceans. However, in general reasonable representation of the monsoon for most models and regions provides confidence in precipitation responses simulated by the models under various GeoMIP forcing scenarios.

5.2. Precipitation and Evaporation Response in Monsoonal Regions

The separation of global monsoon precipitation into its regional components enables an evaluation of the regional hydrologic responses (Figure 12). We only consider the summer season for each region, the time of maximum precipitation (JJA for the Northern Hemisphere and DJF for the Southern Hemisphere).

For the 4xCO_2 experiment, the median response of all the models is an increase in precipitation for both land and ocean, except for the North American monsoon, where a weakening of the monsoon precipitation is evident, in agreement with *Lee and Wang* [2012]. In detail for the 4xCO_2 experiment, a robust increase of precipitation by about 70 mm season^{-1} (10%) occurs over both land and ocean for India and East Asia. A robust decrease of precipitation is simu-

lated for North America with values around 30 mm season^{-1} (7%) over land and around 40 mm season^{-1} (5%) over the ocean.

Evaporation for the 4xCO_2 experiment increases over the ocean and does not change over land for most regions (Figure 12, the two left whiskers symbols of each region). A robust decrease in evaporation over land only occurs for the monsoonal regions of America and South Africa, as overall, the hydrologic cycle strengthens in these simulations. The differences in monsoonal precipitation response over land and ocean in a warming climate and their governing mechanisms are further discussed by *Fasullo* [2010], and arise in part from the land-ocean contrast in warming and a reduction in evaporation due to reduced stomatal conductance in a high CO_2 environment.

For the G1 experiments, a decrease in median precipitation is simulated for all regions except for a zero change for Australia over land (see Figure 12, top and middle panel). In particular, we find a decrease in precipitation over land for East Asia ($\approx$ 40 mm season^{-1}, 6%), North and South America ($\approx$ 30 mm season^{-1}, 7% and 6%, respectively) where all models agree on the sign of the change, and South Africa (7 mm season^{-1}, 5%), where 95% of the models agree on the sign of the change. The relative multi-model median differences between the G1 and 1850 experiment also exceed the interannual variability of G1 (dark red error bars), reported changes are therefore significant. Precipitation is reduced over India by $\approx$ 15 mm season^{-1} (2%), with a reduction simulated for more than 75% of the models. However, due to the large interannual variability the change is not considered to be significant. Also, precipitation changes over the ocean for most regions are not significant due to the large interannual variability.

Departures of the multi-model median precipitation in G1 from the 1850 control over land are much smaller for Australia, West Africa, and Asia, than those of the 4xCO_2, but they are at

least half as large for South Asia. For the other regions, departures of the multi-model median precipitation in G1 are similar for North and South America and South Africa to those of the 4xCO_2 simulation, with North America being the only region that shows a change in the same direction for both experiments. Evaporation over land is strongly decreased for all the models in G1 (Figure 12, bottom panel) with strongest reductions over East Asia, North and South America, and South Africa. The disproportionate cooling of the ocean might allow less moisture to be drawn from the ocean, which may further contribute to the reduction of precipitation and evaporation over land [*Boos and Kuang*, 2010].

The frequency of the precipitation intensity for the 4xCO_2 experiment between the 25th and 75th percentile of the PDF is reduced for all regions and models, whereas heavy precipitation frequency increases (Figure 13), as has also been noted in other recent work [*Chou et al.*, 2012]. In some respects the Asian monsoon is unique as the heating over ocean draws water vapor from the Arabian Sea and the Bay of Bengal to support rainfall over land [*Fasullo*, 2012], which is likely responsible for the increase in precipitation frequency for months that experience heavy precipitation of more than 10 mm day^{-1} over land and ocean (Figure 13, left, first and second row). The increase in heavy precipitation is limited over land for North and South American monsoon domains. For North America, this results in reduction of precipitation for most models, which may be a result of its negligible ocean component and inland location, where moisture is limited and evapotranspiration is reduced.

In contrast to the 4xCO_2 experiment, the geoengineering simulations show an increase in the frequency of small and medium precipitation intensity that coincides with a slight increase in tropical stability, as discussed above. For all regions considered besides India, the frequency of months with medium to heavy precipitation intensity is reduced, with a larger reduction over

land than over the ocean (Figure 13, right). Reductions in the frequency of heavy precipitation over North and South American monsoonal regions are particularly large around 20 – 30% for intensities above the 95th percentile of the distribution.

The spread of the precipitation response across individual models is in general much larger for 4xCO_2 than for G1, suggesting less variability and therefore less uncertainty in the results in signatures of precipitation change in the G1 simulations. Some models are outliers regarding their precipitation and evaporation responses (see Figure 14). The GISS-E2-R model stands out in simulating the largest reduction in evaporation over land for most regions, which is consistent with the largest global precipitation reduction in G1 compared to the other models, as discussed above. EC-Earth and BNU-ESM models show the smallest reduction in evaporation in G1 and the largest increase for the 4xCO_2 experiment over land. For EC-Earth this is consistent with the missing stomatal conductance effect with changing CO_2 concentrations (as discussed above). However, the extreme behavior in evaporation in these models is not reflected in the monsoonal summer precipitation response for most regions. This is because the monsoonal precipitation is influenced by both local and large-scale processes, due to the complex interactions of the different components that contribute to the hydrological cycle.

6. Discussion

The simulated precipitation and evaporation changes in the highly idealized 4xCO_2 and G1 experiments point to the fact that the hydrological cycle would be perceptibly weakened by SRM in comparison to the 1850 control. Precipitation and evaporation are considerably reduced in G1, while departures from the preindustrial control are generally smaller or similar to those that occur in the 4xCO_2 experiment with no geoenginering performed. Further, the expected increase in flooding in a high CO_2 environment, especially over the Asian monsoonal regions,

is reduced in G1. Instead, a reduction in frequency of heavy precipitation, of much smaller but considerable magnitude than in the 4xCO_2 experiment, is simulated in G1 compared to the control.

However, from this analysis it is not clear how simulated changes in the $P - E$ balance are going to impact runoff and soil moisture. These highly uncertain variables depend often on simple parameterizations in climate models [e.g., *Trenberth et al.*, 2003] and improved and more detailed and complex models are necessary to investigate the full impact of SRM on changes in regional soil moisture and aridity, with inherent consequences for vegetation. In addition, more realistic experiments are required to support these findings, for instance future transient model simulations with more realistic forcings as designed in other GeoMIP experiments (G3 and G4, described in *Kravitz et al.* [2011]).

The G1 experiment applies a reduced solar constant to simulate a uniform reduction of the Earth's planetary albedo, which might be achieved by placing mirrors into space [e.g., *Angel*, 2006]. It has to be pointed out that the climate response of such an experiment may be very different from other theoretical experiments where, for instance, stratospheric aerosols are used to reduce the planetary albedo. However, such experiments do not usually provide as large a negative forcing as G1, thereby making them less useful experiments for examining the gross aspects of hydrological sensitivity of interest here. In addition, stratospheric aerosols result in heating of the stratosphere, particularly in the tropics, and this results in dynamic perturbations [e.g., *Stenchikov et al.*, 2002; *Tilmes et al.*, 2009]. Changes in heating rates in the stratosphere and at the tropopause are likely to further influence the tropospheric lapse rate, which may alter relative humidity and the hydrological cycle. Furthermore, changes in stratospheric and tropospheric chemical composition are likely to interact with radiation and dynamics while in

this study the impact of increasing CO_2 concentration with and without SRM on chemistry is not considered. Finally, the interaction of thermal and hydrological changes with biogeochemical cycles (e.g., of carbon, nitrogen) in the land and ocean in the context of SRM is an interesting topic that requires further investigation.

7. Summary

In this study we have explored the robustness of the simulated global and regional response of the hydrologic cycle to a reduction of incoming solar radiation. The solar constant was reduced to counteract the radiative imbalance at the top of the atmosphere from quadrupling of preindustrial CO_2. The hydrologic response of this experiment compared to 1850 conditions is contrasted to the response of a quadrupling CO_2 experiment without solar dimming.

The abrupt increase of CO_2 in both 4xCO_2 and G1 experiments leads to an initial decrease of upwelling latent heat flux at the Earth's surface, mainly controlled by the changes in the increase of atmospheric stability, which has a global impact on evaporation. In addition, changes in evapotranspiration over land strongly affect the precipitation over land. These changes have implications for temperatures, clouds, and precipitation.

The response due to the warming in the 4xCO_2 experiment leads to global precipitation increases of 34 mm a^{-1} (3.6%) over land and 79 mm a^{-1} (6.8%) over the ocean considering the multi-model mean and around 6.2% for the multi-model median. East Asia and India experience a robust precipitation increase of around 10%. On the other hand, a robust regional reduction in precipitation for the North American monsoon of around 7% over land is simulated. The frequency of weak and medium precipitation intensities is generally reduced for monsoonal regions while the frequency of heavy precipitation is strongly increased which likely results in increased aridity and flooding in these regions.

Solar reduction in G1 is found to significantly impact precipitation and evaporation in both the tropics and mid-latitudes. Despite a stabilization of global mean temperatures in G1, the tropics experience a cooling while high latitudes are warming. This results in a robust (in the sense that most models provide the same signature, unlike the 4xCO_2 simulations) global decrease in precipitation of 43 mm a^{-1} (4.5%) over land and 50 mm a^{-1} (4.3%) over the ocean considering the multi-model mean and 3.6% over land and 4.6% over ocean for the multi-model median. Significant changes of precipitation and evaporation are also simulated for mid-latitudes, with a maximum reduction in the 45°N – 65°N band for G1 of 6% over land and 4% over the ocean. For this region, the frequency of monthly precipitation intensity between 3 and 7 mm day^{-1} is reduced by about 30% over land and 25% over the ocean in summer, while changes are much smaller in winter. These changes are generally smaller than the changes produced by the 4xCO_2 forcing.

A detailed analysis of monsoonal precipitation and evaporation provides information about regional impacts of geoengineering. The statistics of total precipitation, monsoonal area, and seasonal cycle performed in the control experiments are in general in good agreement with observational estimates for present day conditions using GPCP and TRMM datasets, besides the delay of the onset of the Indian monsoon over the ocean for most models. Further, the simulated global land to ocean ratio of precipitation is about 7% smaller compared to observations, due to an overestimate of the amount of the precipitation in various monsoonal regions over the ocean during their peak season. Also, observations might underestimate precipitation in those regions [*Stephens et al.*, 2012]. This may have an impact on the response of the climate forcings in different experiments, but cannot be identified for individual model responses.

Considering the multi-model median and the interannual variability of G1, we find a robust and significant decrease of monsoonal precipitation over land for East Asia (6%), North America (7%), South America (6%) and South Africa (5%), and a robust but not significant decrease of 2% over India. These decreases occur primarily in months with larger precipitation intensities (above the 95th percentile of the precipitation distribution) which experience a robust decrease in frequency of about 20% for all monsoonal regions. These changes are in general greater over land than over the ocean. Decreases in evaporation of more than 10% occur over land as compared to 3% over the ocean.

The resulting weakening of the hydrologic cycle due to SRM in comparison to the control reduces precipitation and evaporation over land by a considerable amount globally and especially in most monsoonal regions and in north mid-latitudes. On the other hand, dramatic increases in heavy precipitation globally in the 4xCO_2 experiment and inferred increases in flooding might be prevented by SRM as extreme rainfall intensities are likely to decrease, especially for Asian monsoonal regions, if G1 type geoengineering is to be employed. Changes in soil moisture and implications for agriculture as a result of SRM should be investigated in future studies and more work is needed to assess the positive and negative consequences of this effect on the biosphere and society, using more appropriate models and realistic scenarios. In summary, we have shown that even though global temperatures can be approximately balanced in this experiment, the hydrological cycle does not resume control conditions, even though extreme deviations from the control are in general smaller than in an experiment where no geoengineering is performed.

Appendix A: Importance of an Interactive Land Carbon Cycle to the Surface Energy Budget in CESM4

The importance of changes in stomatal conductance for the surface energy budget due to abrupt CO_2 increase for the 4xCO_2 and G1 experiments is discussed here in the context of additional CCSM4 simulations. Changes during the first year of each GeoMIP simulation (Figure A1) are contrasted to simulations that assume background CO_2 levels in the land componet of the model and therefore ignore the impact of CO_2 on the stomatal conductance (Figure A2).

The responses of surface fluxes of latent heat (LH) and sensible heat (SH), and relative humidity (RH) are very similar in the GeoMIP G1 and 4xCO_2 simulations (Figure A1 and A2), even though the downwelling shortwave (SW) radiation is of opposite sign due to the global decrease in solar intensity in G1. Over land, LH and RH are strongly reduced at most latitudes with the largest absolute changes in LH occurring in the tropics (Figure A1, second row). Further, SH and net LW flux (not shown) over land increase to balance the reduction in LH.

Simulations omitting the response in stomatal conductance reveal the importance of this process (Figure A2). Changes in LH and RH over land are small relative to the GeoMIP simulations including the influence of stomatal conductance (Figure A2, second row). Significant differences are also obvious for the other fields over land. For instance, if the stomatal response is turned off, warming over land is small under G1 conditions (Figure A2, first row), whereas it exceeds 0.5 K when the stomatal response is included (Figure A1, first row), consistent with earlier studies [e.g., *Joshi et al.*, 2008; *Cao et al.*, 2010]. On the other hand, no significant differences over ocean are evident.

Therefore, these simulations suggest that the fast precipitation response over land is strongly influenced by stomatal conductance. A reduction of LH in both 4xCO_2 and G1 experiments is

to a large part controlled by the abrupt reduction of the stomatal conductance of plants due to the increase of CO_2, which in turn impacts temperature, precipitation, and clouds [*Ban-Weiss et al.*, 2011; *Fyfe et al.*, 2013]. For the 4xCO_2 experiment, clouds decrease over land in mid-latitudes but increase markedly in the deep tropics (Figure A1). Increases in the deep tropics appear to be related to warming of the land surface and an overall strengthening of the hydrologic cycle in the 4xCO_2 experiment and a resultant increase in convective instability, rainfall, and large-scale convergence. For G1, changes in clouds are relatively weak throughout most of the tropics, and coincide with an overall weakening of the hydrologic cycle, a reduction in LH flux compared to the 4xCO_2 experiment, which further interacts with the downwelling SW radiation. If the stomatal conductance is not adjusted to high CO_2 concentrations, the initial increase in rainfall over land in the 4xCO_2 experiment (Figure A2 first column, third row) is actually smaller than with the adjustment (Figure A1 first column, third row) for the first year of the simulation, which coincides with less warming over land. Subsequent work is warranted to more fully understand these changes and to investigate the robustness of these results by examining other models.

Acknowledgments. We thank all participants of the Geoengineering Model Intercomparison Project and their model development teams, the CLIVAR/WCRP Working Group on Coupled Modeling for endorsing GeoMIP, and the scientists managing the Earth System Grid data nodes who have assisted with making GeoMIP output available. We further acknowledge the World Climate Research Programme's Working Group on Coupled Modelling, which is responsible for CMIP, and we thank the climate modeling groups for producing and making available their model output. For CMIP the U.S. Department of Energy's Program for Climate Model Diagnosis and Intercomparison provides coordinating support and led development of software infrastructure in partnership with the Global Organization for Earth System Science Portals. We

thank the TRMM Online Visualization and Analysis System (TOVAS) and the GPCC Global Precipitation Climatology Centre for providing the rainfall dataset. The participation of J. Fasullo is supported by NASA Award NNG06GB91G. J. Haywood and A. Jones were supported by the joint DECC/Defra Met Office Hadley Centre Climate Programme (GA01101). K. Alterskjær, D. B. Karam, J. E. Kristjánsson, U. Niemeier, H. Schmidt, and M. Schulz received funding from the European Unions Seventh Framework Programme (FP7/2007-2013) under grant agreement no. 226567-IMPLICC. K. Alterskjær and J. E. Kristjánsson received support from the Norwegian Research Council's Programme for Supercomputing (NOTUR) through a grant of computing time. B. Kravitz is supported by the Fund for Innovative Climate and Energy Research. Simulations performed by B. Kravitz were supported by the NASA High-End Computing (HEC) Program through the NASA Center for Climate Simulation (NCCS) at Goddard Space Flight Center. Computer resources for P. J. Rasch, B. Singh, and J.-H. Yoon, were provided by the National Energy Research Scientific Computing Center, which is supported by the Office of Science of the U.S. Department of Energy under Contract No. DE-AC02-05CH11231. J.-H. Yoon was further supported by the NERSC. D. Ji and J. Moore thank all members of the BNU-ESM model group, as well as the Center of Information and Network Technology at Beijing Normal University for assistance in publishing the GeoMIP dataset. A. Robock is supported by US National Science Foundation grant AGS-1157525. S. Watanabe was supported was supported by SOUSEI Program, MEXT, Japan, and the Earth Simulator was used for the simulations of MIROC-ESM. Finally, we thank Gary Strand for CCSM4 output formatting and James Hurrell for supporting this study. The National Center for Atmospheric Research is funded by the National Science Foundation.

References

Adler, R., G. Huffman, A. Chang, R. Ferraro, P.-P. Xie, J. Janowiak, B. Rudolf, U. Schneider, S. Curtis, D. Bolvin, A. Gruber, J. Susskind, P. Arkin, and E. Nelkin (2003), The Version-2 Global Precipitation Climatology Project (GPCP) monthly precipitation analysis (1979 – present), *Journal of Hydrometeorology*, *4*(January 1997), 1147–1167.

Andrews, T., and P. M. Forster (2010), The transient response of global-mean precipitation to increasing carbon dioxide levels, *Environmental Research Letters*, *5*(2), 025,212, doi: 10.1088/1748-9326/5/2/025212.

Andrews, T., P. M. Forster, and J. M. Gregory (2009), A surface energy perspective on climate change, *Journal of Climate*, *22*(10), 2557–2570, doi:10.1175/2008JCLI2759.1.

Angel, R. (2006), Feasibility of cooling the Earth with a cloud of small spacecraft near the inner Lagrange point (L1), *Proceedings of the National Academy of Sciences of the United States of America*, (103), 17,184–17,189.

Arakawa, A., and W. H. Schubert (1974), Interactions of cumulus cloud ensemble with the large-scale environment, Part I, *J. Atmos. Sci.*, *31*, 674–701.

Bala, G., P. B. Duffy, and K. E. Taylor (2008), Impact of geoengineering schemes on the global hydrological cycle., *Proceedings of the National Academy of Sciences of the United States of America*, *105*(22), 7664–9, doi:10.1073/pnas.0711648105.

Ban-Weiss, G. A., G. Bala, L. Cao, J. Pongratz, and K. Caldeira (2011), Climate forcing and response to idealized changes in surface latent and sensible heat, *Environmental Research Letters*, *6*(3), 034,032, doi:10.1088/1748-9326/6/3/034032.

Bluth, G. J. S., S. D. Doiron, C. C. Schnetzler, A. J. Krueger, and L. S. Walter (1992), Global tracking of the SO_2 clouds from the June, 1991 Mount Pinatubo eruptions, *Geophysical Re-*

search Letters, *19*(2), 151–154.

Boos, W. R., and Z. Kuang (2010), Dominant control of the South Asian monsoon by orographic insulation versus plateau heating., *Nature*, *463*(7278), 218–222, doi:10.1038/nature08707.

Boucher, O., P. R. Halloran, E. J. Burke, M. Doutriaux-Boucher, C. D. Jones, J. Lowe, M. a. Ringer, E. Robertson, and P. Wu (2012), Reversibility in an Earth System model in response to CO_2 concentration changes, *Environmental Research Letters*, *7*(2), 024,013(9pp), doi:10.1088/1748-9326/7/2/024013.

Cao, L., G. Bala, K. Caldeira, R. Nemani, and G. Ban-Weiss (2010), Importance of carbon dioxide physiological forcing to future climate change., *Proceedings of the National Academy of Sciences of the United States of America*, *107*(21), doi:10.1073/pnas.0913000107.

Chou, C., J. D. Neelin, C.-A. Chen, and J.-Y. Tu (2009), Evaluating the Rich-Get-Richer mechanism in tropical precipitation change under global warming, *Journal of Climate*, *22*(8), 1982–2005, doi:10.1175/2008JCLI2471.1.

Chou, C., C.-A. Chen, P.-H. Tan, and K. T. Chen (2012), Mechanisms for global warming impacts on precipitation frequency and intensity, *Journal of Climate*, *25*(9), 3291–3306, doi:10.1175/JCLI-D-11-00239.1.

Crutzen, P. J. (2006), Albedo enhancements by stratospheric sulfur injections: A contribution to resolve a policy dilemma? An Editorial Essay, *Clim. Change*, *77*, 211–219.

Del Genio, A. D., and M.-S. Yao (1993), Efficient cumulus parameterization for long-term climate studies: The GISS scheme. The representation of cumulus convection in numerical models, Meteor. Monogr., *Amer. Meteor. Soc.*, *46*, 181–184.

Doutriaux-Boucher, M., M. J. Webb, J. M. Gregory, and O. Boucher (2009), Carbon dioxide induced stomatal closure increases radiative forcing via a rapid reduction in low cloud, *Geo-*

phys. Res. Lett., *36*, doi:10.1029/2008GL036273.

Durack, P. J., S. E. Wijffels, and R. J. Matear (2012), Ocean salinities reveal strong global water cycle intensification during 1950 to 2000., *Science*, *336*(6080), 455–458, doi:10.1126/science.1212222.

Emanuel, K. (1991), A scheme for representing cumulus convection in large-scale models, *J Atmos Sci*, *48*, 2313–2335.

Emori, S., T. Nozawa, A. Numaguti, and I. Uno (2001), Importance of cumulus parameterization for precipitation simulation over East Asia in june., *Journal of the Meteorological Society of Japan*, *79*(4), 939–947, doi:10.2151/jmsj.79.939.

Fasullo, J. (2012), A mechanism for land - ocean contrasts in global monsoon trends in a warming climate, *Climate Dynamics*, *39*(5), 1137–1147, doi:10.1007/s00382-011-1270-3.

Fasullo, J. T. (2010), Robust land-ocean contrasts in energy and water cycle feedbacks, *Journal of Climate*, *23*(17), 4677–4693, doi:10.1175/2010JCLI3451.1.

Fasullo, J. T., and K. E. Trenberth (2012), A less cloudy future: the role of subtropical subsidence in climate sensitivity., *Science (New York, N.Y.)*, *338*(6108), 792–4, doi:10.1126/science.1227465.

Fyfe, J., J. Cole, V. Arora, and J. Scinocca (2013), Biogeochemical carbon coupling influences global precipitation in geoengineering experiments, *Geophysical Research Letters*, p. in press, doi:10.1002/grl.50166.

Govindasamy, B., and K. Caldeira (2000), Geoengineering Earth's radiation balance to mitigate CO_2-induced climate change, *Geophys. Res. Lett.*, *27*(14), 2141–2144.

Govindasamy, B., K. Caldeira, and P. Duffy (2003), Geoengineering Earth's radiation balance to mitigate climate change from a quadrupling of CO_2, *Global and Planetary Change*, *37*(1-2),

157–168, doi:10.1016/S0921-8181(02)00195-9.

Gregory, D., and R. Powntree, P. (1990), A mass flux convection scheme with representation of cloud ensemble characteristics and stability-dependent closure, *Monthly Weather Review*, *118*, 1483–1506.

Gregory, J. M., W. J. Ingram, M. A. Palmer, G. S. Jones, P. A. Stott, R. B. Thorpe, J. A. Lowe, T. C. Johns, and K. D. WIlliams (2004), A new method for diagnosing radiative forcing and climate sensitivity, *Geophysical Research Letters*, *31*, L03,205, doi:10.1029/2003GL018747.

Hansen, G., T. Svenø e, M. P. Chipperfield, A. Dahlback, and U.-P. Hoppe (1997), Evidence of substantial ozone depletion in winter 1995/96 over Northern Norway, *Geophys. Res. Lett.*, *24*, 799–802.

Haywood, J. M., A. Jones, N. Bellouin, and D. Stephenson (2013), Asymmetric forcing from stratospheric aerosols impacts Sahelian rainfall, *Nature Climate Change*, doi: 10.1038/NCLIMATE1857.

Heckendorn, P., D. Weisenstein, S. Fueglistaler, B. P. Luo, E. Rozanov, M. Schraner, L. W. Thomason, and T. Peter (2009), The impact of geoengineering aerosols on stratospheric temperature and ozone, *Environmental Research Letters*, *4*, 045,108, doi:10.1088/1748-9326/4/4/045108.

Hegerl, G. C., and S. Solomon (2010), Climate change. Risks of climate engineering., *Science*, *325*(5943), 955–956, doi:10.1126/science.1178530.

Held, I. M., and B. Soden (2006), Robust responses of the hydrological cycle to global warming, *Journal of Climate*, *19*, 5686–5699.

Hsu, P.-C., T. Li, H. Murakami, and A. Kitoh (2013), Future change of the global monsoon revealed from 19 CMIP5 models, *Journal of Geophysical Research*, *118*(November 2012),

779 1–14, doi:10.1002/jgrd.50145.

780 Huffman, G. J., R. F. Adler, D. T. Bolvin, and G. Gu (2009), Improving the global precip-
781 itation record: GPCP Version 2.1, *Geophysical Research Letters*, *36*(17), L17,808, doi:
782 10.1029/2009GL040000.

783 Irvine, P. J., A. Ridgwell, and D. J. Lunt (2010), Assessing the regional disparities in geoengi-
784 neering impacts, *Geophysical Research Letters*, *37*(18), doi:10.1029/2010GL044447.

785 Jones, A., J. Haywood, O. Boucher, B. Kravitz, and A. Robock (2010), Geoengineering by
786 stratospheric SO_2 injection: results from the Met Office HadGEM2 climate model and com-
787 parison with the Goddard Institute for Space Studies ModelE, *Atmospheric Chemistry and*
788 *Physics*, *10*(13), 5999–6006, doi:10.5194/acp-10-5999-2010.

789 Joshi, M. M., J. M. Gregory, M. J. Webb, D. M. H. Sexton, and T. C. Johns (2008), Mechanisms
790 for the land/sea warming contrast exhibited by simulations of climate change, *Climate Dyn.*,
791 *30*, 455–465.

792 Kharin, V. V., F. W. Zwiers, X. Zhang, and G. C. Hegerl (2007), Changes in temperature and
793 precipitation extremes in the IPCC ensemble of global coupled model simulations, *Journal of*
794 *Climate*, *20*(8), 1419–1444, doi:10.1175/JCLI4066.1.

795 Kravitz, B., and A. Robock (2011), Climate effects of high-latitude volcanic eruptions:
796 Role of the time of year, *Journal of Geophysical Research*, *116*(D1), D01,105, doi:
797 10.1029/2010JD014448.

798 Kravitz, B., A. Robock, O. Boucher, H. Schmidt, K. E. Taylor, G. Stenchikov, and M. Schulz
799 (2011), The Geoengineering Model Intercomparison Project (GeoMIP), *Atmospheric Science*
800 *Letters*, *12*(2), 162–167, doi:10.1002/asl.316.

Kravitz, B., K. Caldeira, O. Boucher, A. Robock, et al. (2013), Climate model response from the Geoengineering Model Intercomparison Project (GeoMIP), *Journal of Geophysical Research*, (submitted).

Lambert, F. H., M. J. Webb, and M. M. Joshi (2011), The relationship between land ocean surface temperature contrast and radiative forcing, *Journal of Climate*, *24*(13), 3239–3256, doi:10.1175/2011JCLI3893.1.

Launder, B., and J. Thompson (Eds.) (2009), *Geo-Engineering Climate Change: Environmental Necessity or Pandora's Box?*, Cambridge University Press.

Lee, J.-Y., and B. Wang (2012), Future change of global monsoon in the CMIP5, *Climate Dynamics*, (October), doi:10.1007/s00382-012-1564-0.

Lin, J.-L. (2007), The double-ITCZ problem in IPCC AR4 coupled GCMs: Ocean - atmosphere feedback analysis, *J. Climate*, *20*, 4497–4525.

Liu, X., R. C. Easter, S. J. Ghan, R. Zaveri, P. Rasch, X. Shi, J.-F. Lamarque, a. Gettelman, H. Morrison, F. Vitt, a. Conley, S. Park, R. Neale, C. Hannay, a. M. L. Ekman, P. Hess, N. Mahowald, W. Collins, M. J. Iacono, C. S. Bretherton, M. G. Flanner, and D. Mitchell (2012), Toward a minimal representation of aerosols in climate models: description and evaluation in the Community Atmosphere Model CAM5, *Geoscientific Model Development*, *5*(3), 709–739, doi:10.5194/gmd-5-709-2012.

Lunt, D. J., A. Ridgwell, P. J. Valdes, and A. Seale (2008), Sunshade World: A fully coupled GCM evaluation of the climatic impacts of geoengineering, *Geophysical Research Letters*, *35*(12), L12,710, doi:10.1029/2008GL033674.

Neale, R. B., J. H. Richter, and M. Jochum (2008), The impact of convection on ENSO: From a delayed oscillator to a series of events, *Journal of Climate*, *21*(22), 5904–5924, doi:

824 10.1175/2008JCLI2244.1.

825 Neelin, J. D., O. Peters, and K. Hales (2009), The transition to strong convection, *Journal of the*
826 *Atmospheric Sciences*, *66*(8), 2367–2384, doi:10.1175/2009JAS2962.1.

827 Nordeng, T. E. (1994), Extended versions of the convective parameterization scheme at
828 ECMWF and their impact on the mean and transient activity of the model in the tropics,
829 *Technical Memorandum*, European Centre for Medium-Range Weather Forecasts.

830 O'Gorman, P., and T. Schneider (2009), The physical basis for increases in precipitation ex-
831 tremes in simulations of 21st-century climate change, *Proceedings of the National Academy*
832 *of Sciences of the United States of America*, *106*(35), 14,773–14,777.

833 O'Gorman, P. A. (2012), Sensitivity of tropical precipitation extremes to climate change, *Nature*
834 *Geoscience*, *5*(10), 697–700, doi:10.1038/ngeo1568.

835 Park, S., and C. S. Bretherton (2009), The University of Washington shallow convection and
836 moist turbulence schemes and their impact on climate simulations with the Community At-
837 mosphere Model, *Journal of Climate*, *22*(12), 3449–3469, doi:10.1175/2008JCLI2557.1.

838 Pongratz, J., D. B. Lobell, L. Cao, and K. Caldeira (2012), Crop yields in a geoengineered
839 climate, *Nature Climate Change*, *2*(2), 101–105, doi:10.1038/nclimate1373.

840 Rasch, P. J., S. Tilmes, R. P. Turco, A. Robock, L. Oman, C.-C. Chen, G. L. Stenchikov, and
841 R. R. Garcia (2008), An overview of geoengineering of climate using stratospheric sulphate
842 aerosols, *Philosophical transactions. Series A, Mathematical, physical, and engineering sci-*
843 *ences*, *366*(1882), 4007–37, doi:10.1098/rsta.2008.0131.

844 Richter, J., and P. J. Rasch (2008), Effects of convective momentum transport on the atmospheric
845 circulation in the Community Atmosphere Model, Version 3, *J. Climate*, *21*, 1487–1499, doi:
846 http://dx.doi.org/10.1175/2007JCLI1789.1.

Robock, A., L. Oman, and G. L. Stenchikov (2008), Regional climate responses to geoengineering with tropical and Arctic SO_2 injections, *Journal of Geophysical Research*, *113*(D16), D16,101, doi:10.1029/2008JD010050.

Scheff, J., and D. M. W. Frierson (2012), Robust future precipitation declines in CMIP5 largely reflect the poleward expansion of model subtropical dry zones, *Geophysical Research Letters*, *39*(18), doi:10.1029/2012GL052910.

Schmidt, H., K. Alterskjæ r, D. Bou Karam, O. Boucher, A. Jones, J. E. Kristjánsson, U. Niemeier, M. Schulz, A. Aaheim, F. Benduhn, M. Lawrence, and C. Timmreck (2012), Solar irradiance reduction to counteract radiative forcing from a quadrupling of CO_2: Climate responses simulated by four earth system models, *Earth System Dynamics*, *3*(1), 63–78, doi:10.5194/esd-3-63-2012.

Seager, R., N. Naik, and G. A. Vecchi (2010), Thermodynamic and dynamic mechanisms for large - scale changes in the hydrological cycle in response to global warming, *Journal of Climate*, *23*(17), 4651–4668, doi:10.1175/2010JCLI3655.1.

Seth, A., S. A. Rauscher, M. Rojas, A. Giannini, and S. J. Camargo (2010), Enhanced spring convective barrier for monsoons in a warmer world?, *Climatic Change*, *104*(2), 403–414, doi:10.1007/s10584-010-9973-8.

Soden, B. J., R. T. Wetherald, G. L. Stenchikov, and A. Robock (2002), Global cooling after the eruption of Mount Pinatubo: A test of climate feedback by water vapor, *Science*, *296*, 5568, doi:10.1126/science.296.5568.727.

Solomon, S., D. Qin, M. Manning, M. Marquis, K. Averyt, M. M. B. Tignor, H. L. Miller, and Z. Chen (Eds.) (2007), *Climate Change 2007: The Physical Science Basis. Contribution of Working Group I to the Fourth Assessment Report of the Intergovernmental Panel on Climate*

Change, 996 pp., Cambridge University Press, Cambridge, UK and New York, NY, USA.

Sperber, K. R., H. Annamalai, I.-S. Kang, A. Kitoh, A. Moise, A. Turner, B. Wang, and T. Zhou (2012), The Asian summer monsoon: an intercomparison of CMIP5 vs. CMIP3 simulations of the late 20th century, *Climate Dynamics*, (2), doi:10.1007/s00382-012-1607-6.

Stenchikov, G., A. Robock, V. Ramaswamy, M. D. Schwarzkopf, K. Hamilton, and S. Ramachandran (2002), Arctic Oscillation response to the 1991 Mount Pinatubo eruption: Effects of volcanic aerosols and ozone depletion, *Journal of Geophysical Research*, *107*(D24), 4803, doi:10.1029/2002JD002090.

Stephens, G. L., J. Li, M. Wild, C. A. Clayson, N. Loeb, S. Kato, T. L'Ecuyer, P. W. Stackhouse, M. Lebsock, and T. Andrews (2012), An update on Earth's energy balance in light of the latest global observations, *Nature Geoscience*, *5*(10), 691–696, doi:10.1038/ngeo1580.

Sun, Y., S. Solomon, A. Dai, and R. W. Portmann (2007), How often will it rain?, *Journal of Climate*, *20*(19), 4801–4818, doi:10.1175/JCLI4263.1.

Sutton, R. T., B. Dong, and J. M. Gregory (2007), Land/sea warming ratio in response to climate change: IPCC AR4 model results and comparison with observations, *Geophysical Research Letters*, *34*(2), L02,701, doi:10.1029/2006GL028164.

Taylor, K. E., R. J. Stouffer, and G. A. Meehl (2012), An Overview of CMIP5 and the experiment design, *Bulletin of the American Meteorological Society*, *93*(4), 485–498, doi:10.1175/BAMS-D-11-00094.1.

Tiedtke, M. (1989), A comprehensive mass flux scheme for cumulus parameterization in large-scale models, *Mon. Wea. Rev.*, *117*, 1779–1800.

Tilmes, S., R. Müller, and R. Salawitch (2008), The sensitivity of polar ozone depletion to proposed geoengineering schemes., *Science*, *320*(5880), 1201–1204, doi:

893 10.1126/science.1153966.

894 Tilmes, S., R. R. Garcia, D. E. Kinnison, A. Gettelman, and P. J. Rasch (2009), Impact of geo-
895 engineered aerosols on the troposphere and stratosphere, *Journal of Geophysical Research*,
896 *114*(D12), D12,305, doi:10.1029/2008JD011420.

897 Trenberth, K. E. (1999), Conceptual framework for changes of extremes of the hydrological
898 cycle with climate change, *Climate Change*, *42*, 327–339.

899 Trenberth, K. E., and A. Dai (2007), Effects of Mount Pinatubo volcanic eruption on the hydro-
900 logical cycle as an analog of geoengineering, *Geophysical Research Letters*, *34*(15), L15,702,
901 doi:10.1029/2007GL030524.

902 Trenberth, K. E., A. Dai, R. M. Rasmussen, and D. B. Parsons (2003), The changing character
903 of precipitation, *Bull. Amer. Meteor. Soc.*, *84*, 1205–1217.

904 von Salzen, K., J. F. Scinocca, N. A. McFarlane, J. Li, J. N. S. Cole, D. Plummer, M. C. Reader,
905 X. Ma, M. Lazare, and L. Solheim (2013), The Canadian Fourth Generation Atmospheric
906 Global Climate Model (CanAM4). Part I: Physical processes, *Atmosphere-Ocean*. *51*, 104–
907 125.

908 Wang, B., and Q. Ding (2006), Changes in global monsoon precipitation over the past 56 years,
909 *Geophysical Research Letters*, *33*(6), L06,711, doi:10.1029/2005GL025347.

910 Wigley, T. M. (2006), A combined mitigation/geoengineering approach to climate stabilization,
911 *Science*, *314*, 452–454.

912 Xie, S.-P., C. Deser, G. a. Vecchi, J. Ma, H. Teng, and A. T. Wittenberg (2010), Global warming
913 pattern formation: Sea surface temperature and rainfall, *J. Climate*, *23*, 966–986, doi:oi:
914 http://dx.doi.org/10.1175/2009JCLI3329.1.

915 Zhang, G. J., and N. A. McFarlane (1995), Sensitivity of climate simulations to the parameter-
916 ization of cumulus convection in the Canadian Climate Centre General Circulation Model,
917 *Atmosphere-Ocean*, *33*(3), 407–446.
918 Zhang, G. J., and M. Mu (2005), Effects of modifications to the Zhang-McFarlane convection
919 parameterization on the simulation of the tropical precipitation in the National Center for
920 Atmospheric Research Community Climate Model, Version 3, *J. Geophys. Res.*, *110*, doi:
921 10.1029/2004JD005617.
922 Zheng, Y., J.-L. Lin, and T. Shinoda (2012), The equatorial Pacific cold tongue simulated by
923 IPCC AR4 coupled GCMs: Upper ocean heat budget and feedback analysis, *Journal of Geo-*
924 *physical Research*, *117*(C5), C05,024, doi:10.1029/2011JC007746.

Table 1. Global temperature response (in K) and solar constant reduction of the 12 GeoMIP models, summarized in *Kravitz et al.* [2013]. First ten years of each 4xCO_2 ensemble are disregarded in the values shown here.

Model	4xCO_2 years	G1 years	4xCO_2 minus 1850	G1 minus 4xCO_2	G1 minus 1850	Solar Reduction (W/m^2)
BNU-ESM	150	102	5.71	-5.08	0.63	3.8%
CanESM2	150	300	5.42	-5.41	0.01	4.0%
CESM-CAM5.1-FV	150	59	4.82	-5.02	-0.21	4.7%
CCSM4	255	150	4.48	-4.26	0.22	4.1%
EC-EARTH DMI	50	50	4.38	-4.32	0.06	4.3%
GISS-E2-R	210	210	2.86	-3.16	-0.30	4.5%
HadGEM2-ES	75	70	5.19	-5.07	0.12	3.9%
HadCM3	149	98	5.11	-5.04	0.07	4.1%
IPSL-CM5A-LR	260	50	5.59	-5.50	0.10	3.5%
MIROC-ESM	150	52	5.91	-6.13	-0.22	5.0%
MPI-ESM-LR	150	70	5.36	-5.40	-0.04	4.7%
NorESM1-M	150	50	3.76	-3.79	-0.02	4.0%

Table 2. Convection schemes of different GeoMIP models

Model	Convection Scheme
BNU-ESM	based on *Zhang and McFarlane* [1995] convection scheme [*Zhang and Mu*, 2005]
CanESM2	separated deep moist (bulk mass flux) scheme and shallow moist convection scheme [*von Salzen et al.*, 2013]
CESM-CAM5.1-FV	same deep convection scheme as in CCSM4, but with updated shallow convection scheme [*Park and Bretherton*, 2009]
CCSM4	deep convection is treated by the *Zhang and McFarlane* [1995] scheme, with improvements due to *Richter and Rasch* [2008] and *Neale et al.* [2008]
EC-EARTH DMI	bulk mass flux scheme for deep shallow and mid-level convection *Tiedtke* [1989] with updates (http://www.ecmwf.int/research/ifsdocs/CY33r1/PHYSICS/IFSPart4.pdf)
GISS-E2-R	mass flux approach to cumulus parameterization with one undiluted and one entraining plume, similar to *Del Genio and Yao* [1993]
HadGEM2-ES	mass-flux convection scheme with representation of cloud ensemble characteristics and stability-dependent closure [*Gregory and Powntree, P.*, 1990].
HadCM3	mass flux convection scheme with representation of cloud ensemble characteristics and stability-dependent closure [*Gregory and Powntree, P.*, 1990]
IPSL-CM5A-LR	deep convection scheme using the episodic mixing and buoyancy sorting Emanuel scheme [*Emanuel*, 1991].
MIROC-ESM	modified version of the *Arakawa and Schubert* [1974] scheme [*Emori et al.*, 2001]
MPI-ESM-LR	bulk mass flux scheme for deep shallow and mid-level convection [*Tiedtke*, 1989] with modifications for penetrative convection according to *Nordeng* [1994].
NorESM1-M	deep convection is treated by the *Zhang and McFarlane* [1995] scheme, with improvements due to *Richter and Rasch* [2008] and *Neale et al.* [2008]

Table 3. Global averaged precipitation with global, land, and ocean averages (in mm d^{-1}) for 1850 control simulations and percent change of global precipitation of 4xCO_2 and G1 simulations compared to the 1850 control case. Estimates from Global Precipitation Climatology Project (GPCP) dataset (between 1979 and 2010) [*Adler et al.*, 2003] are 2.60 $\pm$ 0.03 mm d^{-1} globally, 2.45 $\pm$ 0.05 mm day^{-1} over land and 2.76 $\pm$ 0.03 mm day^{-1} over the ocean.

Model	1850 (mm day^{-1})			4xCO_2 (% change)			G1 (% change)		
	global	land	ocean	global	land	ocean	global	land	ocean
BNU-ESM	3.01	2.90	3.22	7.5	6.9	6.3	-1.9	-1.4	-2.5
CanESM2	2.74	2.13	3.08	7.4	2.2	7.6	-4.7	-6.9	-4.2
CESM-CAM5.1-FV	3.03	2.59	3.31	6.7	8.7	5.2	-5.7	-5.3	-5.6
CCSM4	2.93	2.85	3.12	6.3	8.0	4.9	-4.6	-2.1	-5.2
EC-EARTH DMI	2.84	2.40	3.13	7.1	6.1	6.8	-3.3	-2.8	-3.4
GISS-E2-R	3.17	3.01	3.40	1.7	-5.4	3.6	-6.4	-10.5	-4.6
HadGEM2-ES	3.09	2.70	3.43	4.9	-1.1	6.3	-4.3	-3.1	-4.7
HadCM3	2.87	2.58	3.11	4.5	-2.2	5.8	-4.6	-3.6	-4.8
IPSL-CM5A-LR	2.66	2.27	3.00	11.4	7.9	12.4	-6.1	-10.1	-4.3
MIROC-ESM	2.80	2.74	2.93	10.6	3.7	11.0	-3.1	-3.7	-2.8
MPI-ESM-LR	2.92	2.30	3.26	8.7	1.9	9.5	-3.8	-2.5	-3.9
NorESM1-M	2.81	2.76	2.97	5.0	7.4	3.5	-5.1	-2.9	-6.0
Model Mean	2.91	2.60	3.16	6.7	3.6	6.8	-4.5	-4.5	-4.3
GPCP (present)	2.60	2.45	2.76						

Table 4. Global land/ocean precipitation ratio for 1850 control, 4xCO_2 and G1 simulations and estimates from Global Precipitation Climatology Project (GPCP) dataset [*Adler et al.*, 2003].

Model	1850	4xCO_2	G1
BNU-ESM	0.90	0.91	0.91
CanESM2	0.69	0.66	0.67
CESM-CAM5.1-FV	0.78	0.81	0.78
CCSM4	0.92	0.94	0.95
EC-EARTH DMI	0.77	0.76	0.77
GISS-E2-R	0.89	0.81	0.83
HadGEM2-ES	0.79	0.73	0.80
HadCM3	0.83	0.77	0.84
IPSL-CM5A-LR	0.76	0.72	0.71
MIROC-ESM	0.94	0.87	0.93
MPI-ESM-LR	0.71	0.66	0.72
NorESM1-M	0.93	0.96	0.96
Model Mean	0.82	0.80	0.82
GPCP (present)	0.89		

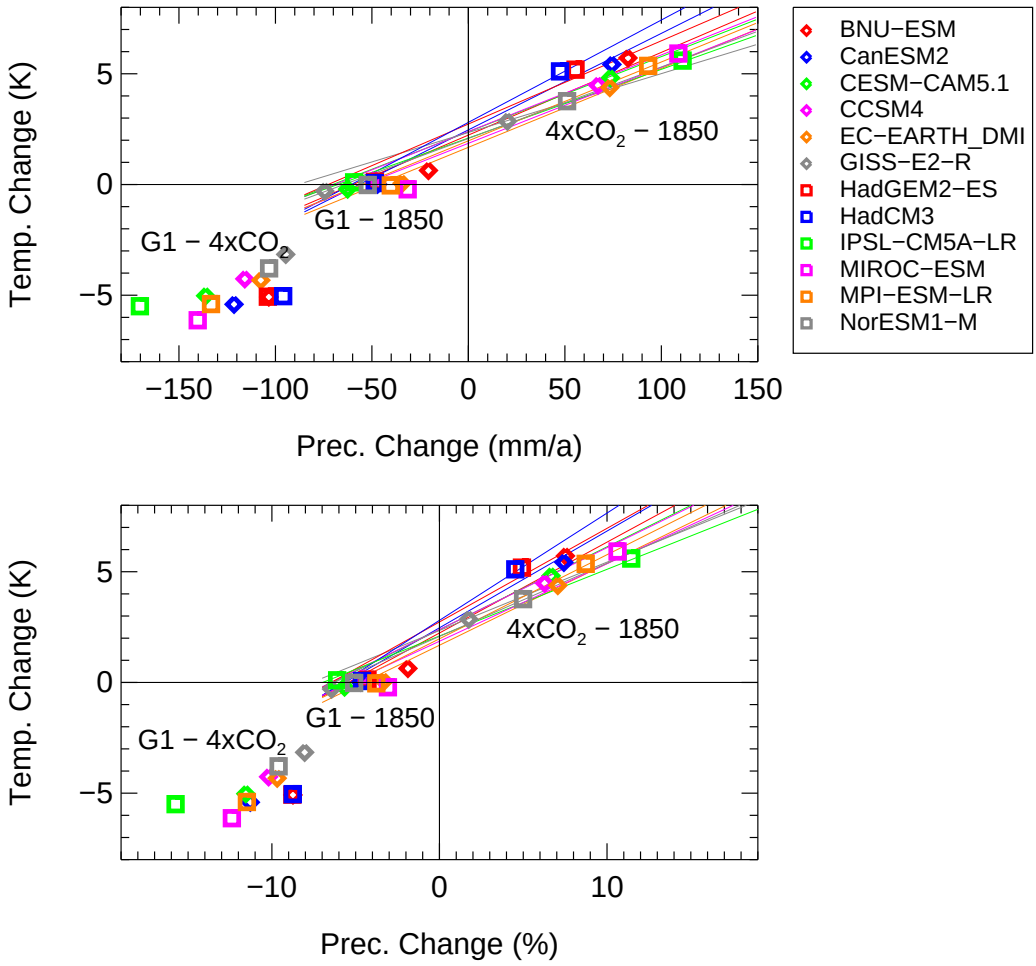

Figure 1. Annual and global averages of absolute (top) and relative (bottom) precipitation response to change in temperature for three cases: $4\mathrm{xCO_2}$ – 1850, G1 – $4\mathrm{xCO_2}$, and G1 – 1850. All symbols are averages over all available ensemble members for each model and all years, besides the first 10 for the $4\mathrm{xCO_2}$ experiment, see text and Table 1. For each model a linear fit (colored line) is derived from the precipitation response for the $4\mathrm{xCO_2}$ experiment compared to 1850 conditions based on the results of the first 10 years of each simulation.

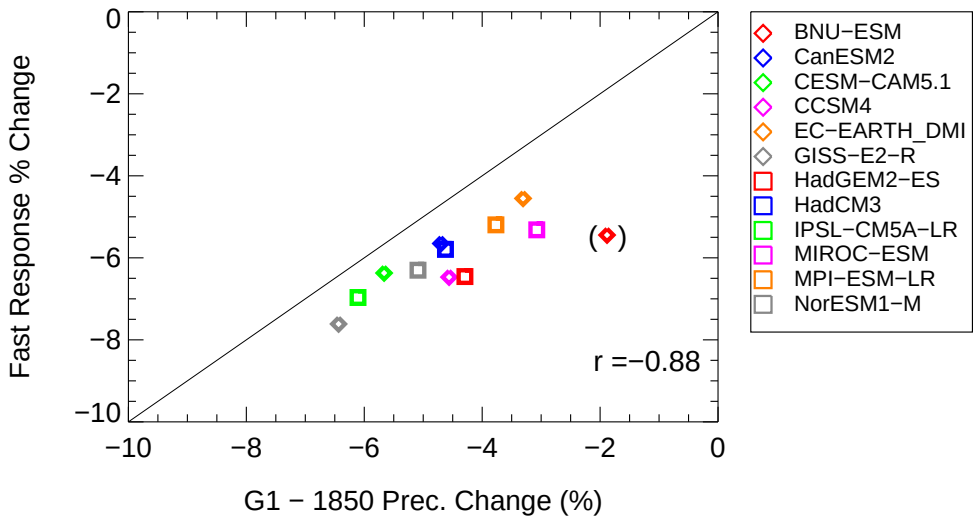

Figure 2. Fast precipitation response (see text) in relative terms derived from Figure 1 (bottom panel) versus precipitation change for G1 – 1850 for different models (colored symbols). The correlation of these values (lower right corner) is derived while ignoring the BNU-ESM model (see text for further details).

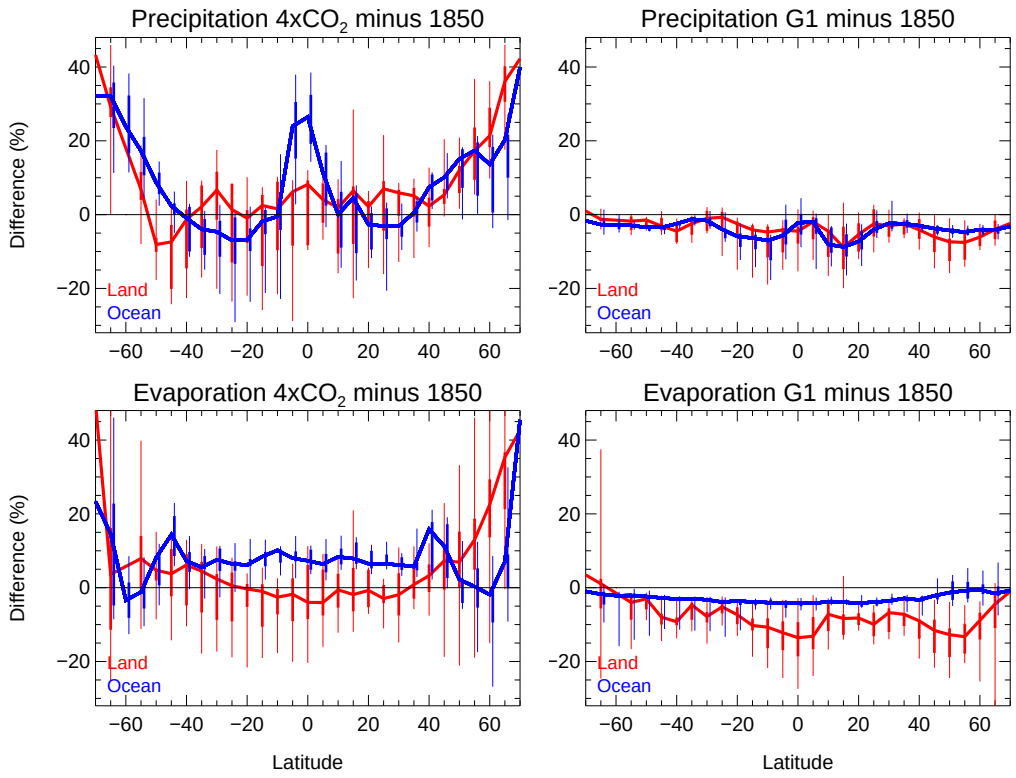

Figure 3. Annually averaged multi-model median zonal changes over land (red solid line) and over the ocean (blue solid line) between 4xCO_2 (left) and G1 (right) experiments with regard to 1850 conditions for the following variables: relative changes in precipitation (top) and evaporation (bottom). The multi-model ranges of the 5th and 95th percentile are illustrated as thin vertical lines, the 25th and 75th percentile as vertical thicker lines.

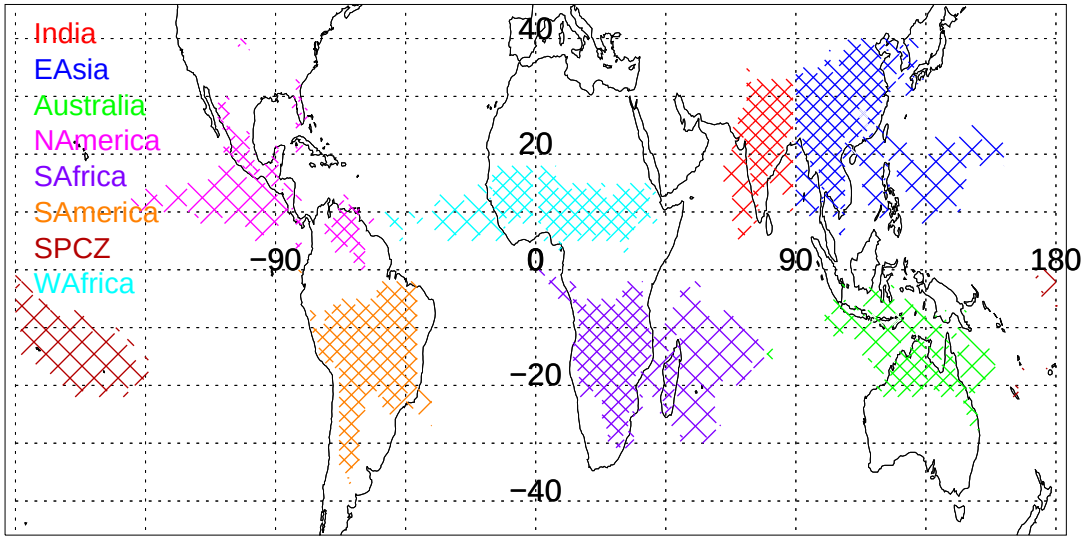

Figure 4. Monsoonal regions (different colors) over land (small hashes) and ocean (large hashes), derived from the Global Precipitation Climatology Project (GPCP) dataset [*Adler et al.*, 2003], covering the years 1979 to 2010, and using criteria described in *Wang and Ding* [2006], see text for more details. The North and South American monsoon are defined here as the American monsoon North and South of the equator, respectively.

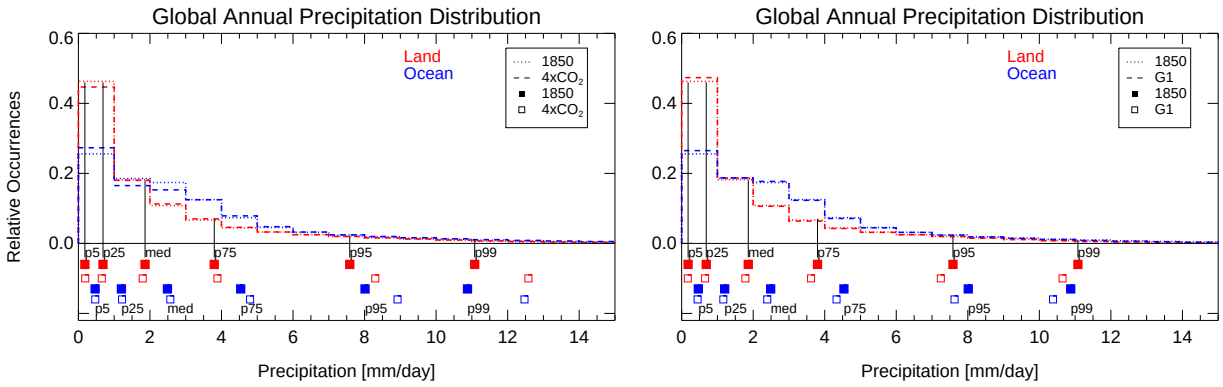

Figure 5. Illustration of statistics for annually averaged multi-model mean probability density function (PDF) of precipitation for land (red) and ocean (blue). The PDF for the 1850 control experiment is shown as dotted lines, the PDF for the 4xCO_2 (left column) and G1 (right column) experiments are shown as dashed lines. The statistics of each distribution are described in median and percentiles for each PDF. As an example, the median and percentiles of the PDF for 1850 over land (red dotted line) are marked as black lines in both panels. The corresponding values are illustrated as red filled squares in the lower part of the figure. Corresponding values for the ocean are shown as blue filled squares, and open colored squares for the other distributions (4xCO_2 PDF: left, G1 PDF: right).

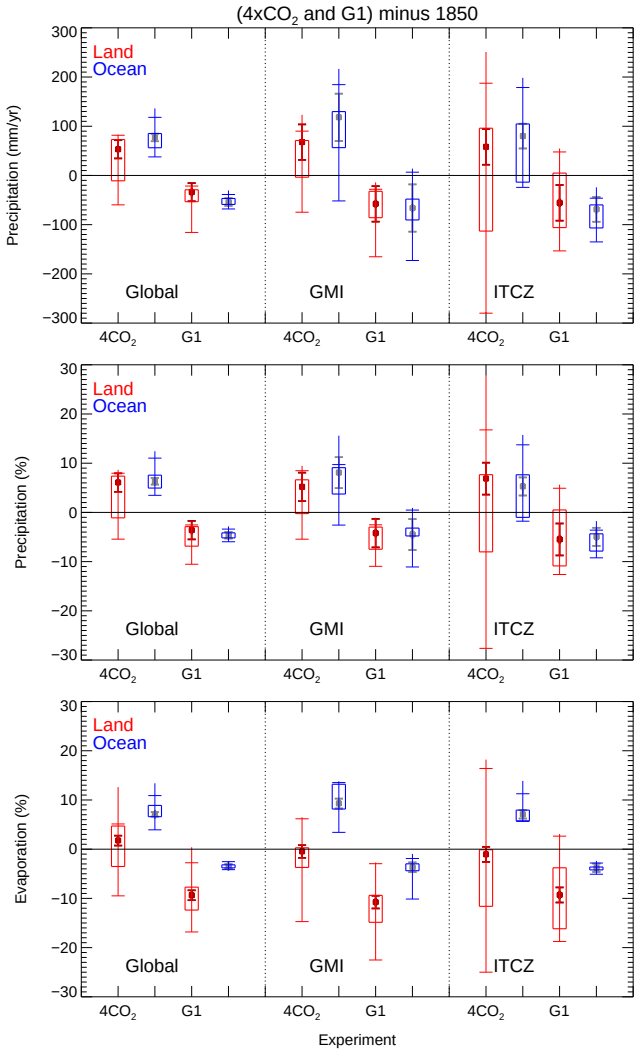

Figure 6. Annually averaged absolute (top) and relative change of precipitation (middle) and evaporation (bottom) for 4xCO_2 and G1 with regard to 1850 conditions. Results are for land (red) and ocean (blue) and for different regions: global (left), global monsoon index (GMI) (middle) and ITCZ averages (right). The multi-model range is illustrated by a vertical line, the 25th and 75th percentile of multi-model results are illustrated as a colored box, and the 5th and 95th percentile are illustrated as horizontal bars. In addition, the multi-model median is shown as solid symbols and the the interannual variability of each experiment, represented by the median standard deviation of annual averages for each model, is show as error bars pointing off the median of the multi-model results (dark red for land and grey for ocean). The two left whisker plots for each region indicate the 4xCO_2 statistics. The two rightmost whiskers plots indicate the G1 statistics.

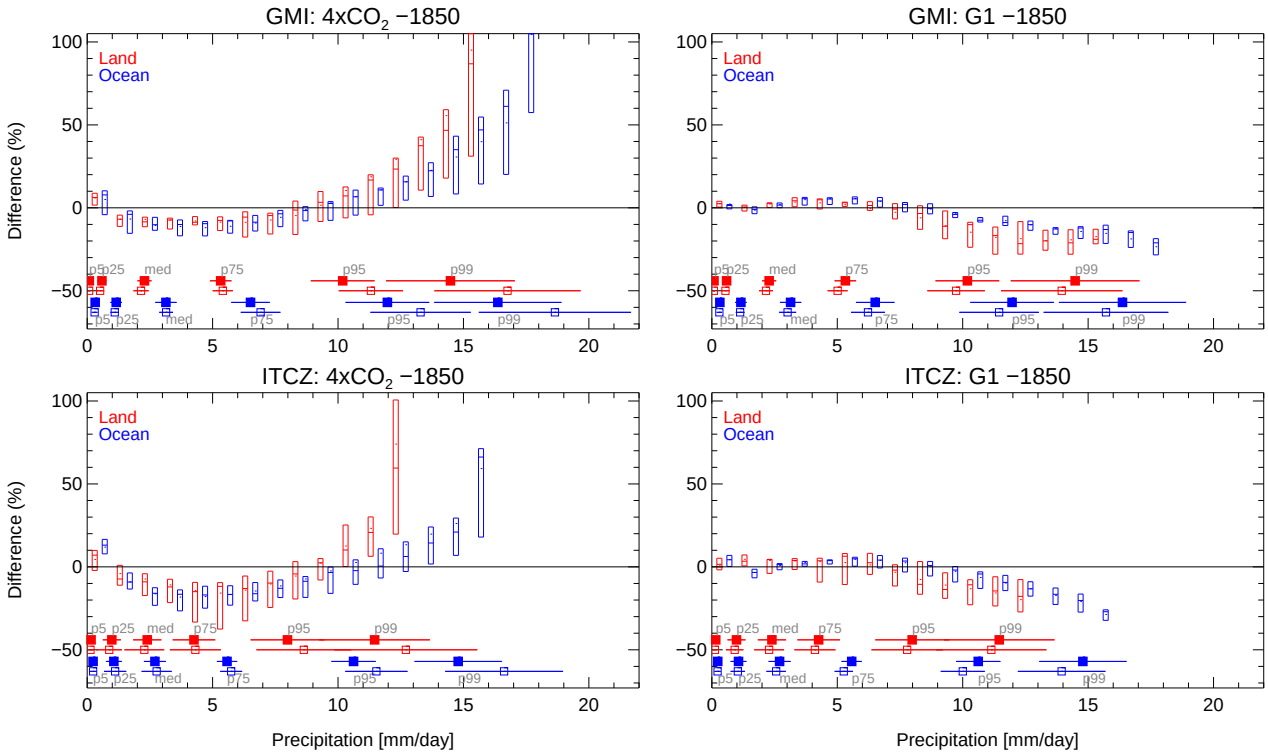

Figure 7. Percent differences of global precipitation frequencies of annually averaged multi-model results for 4xCO_2 simulations (left) and G1 simulations (right) with regard to 1850 conditions based on monthly output. Results are for land (red) and ocean (blue) and for different regions consistent with Figure 6. The multi-model median (horizontal line) and the 25th and 75th percentile (box) are illustrated for 1 mm day^{-1} precipitation increments. Due to the small fraction of the PDFs that occur for very large precipitation events, relative changes of all the bins covering precipitation events above the 99th percentile are combined into one in this analysis. Statistics of the precipitation distributions of each experiment are added, as shown in Figure 5. The range of the results from different models (standard deviation) is shown as horizontal error bars.

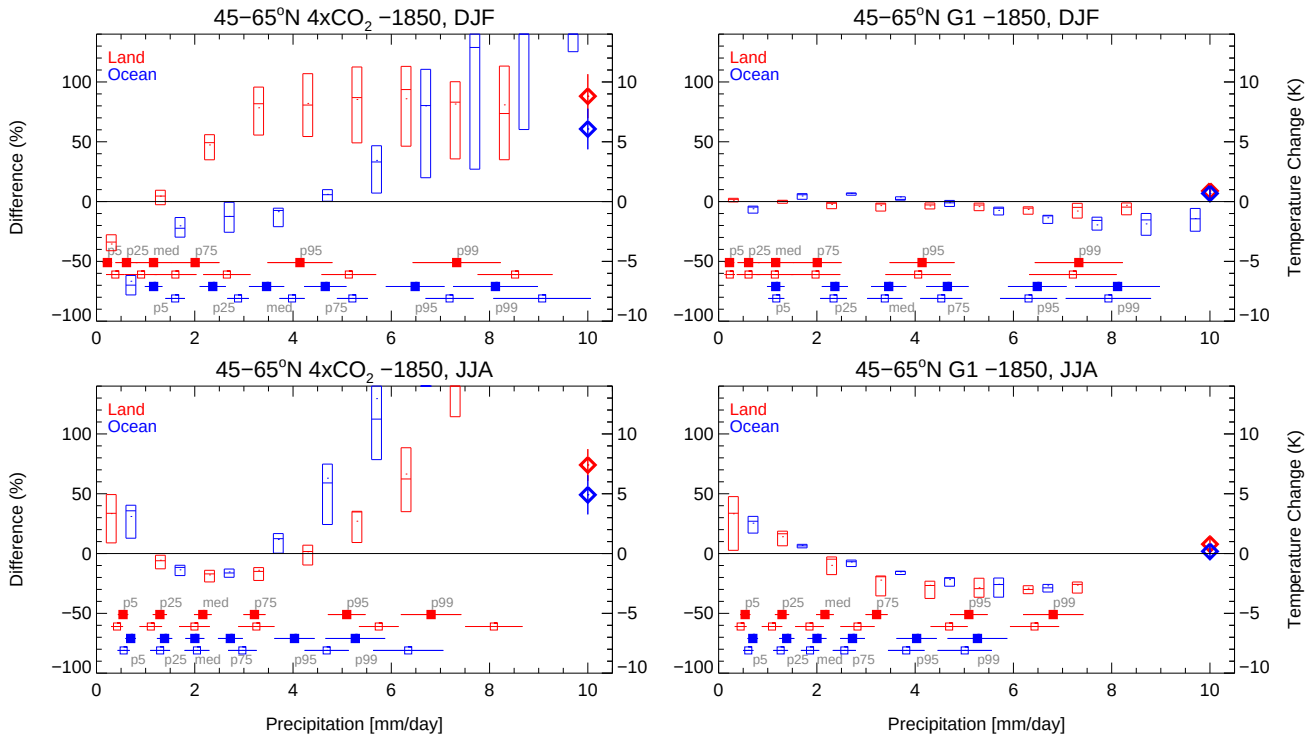

Figure 8. As Figure 7, but for seasonal and zonal averages between 45°N – 65°N for winter (DJF) and summer (JJA). In addition, temperature changes of seasonal and zonal averages are shown as colored diamonds on the right of each plot, the range of different models (standard deviation) is shown as an error bar.

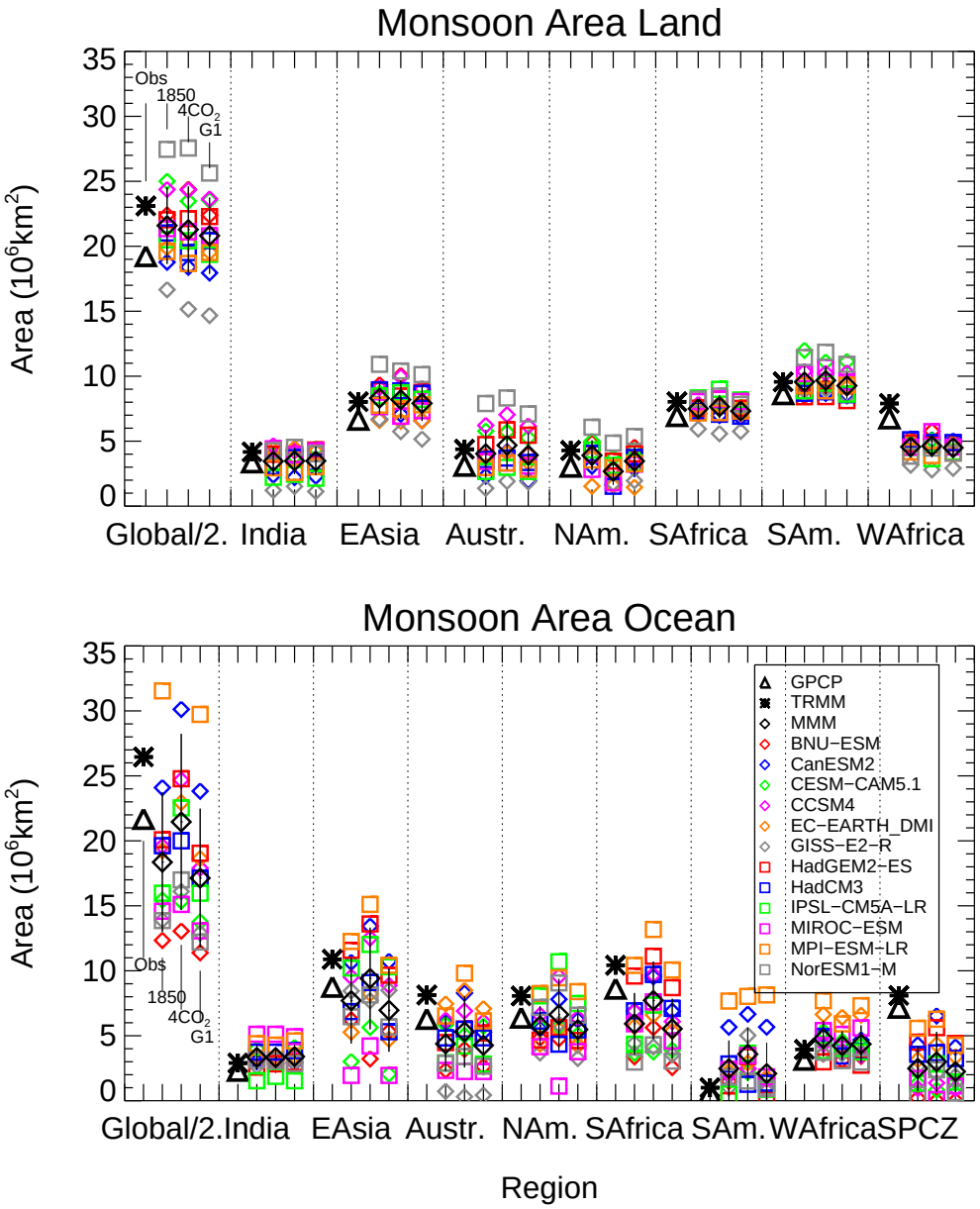

Figure 9. Areas of monsoonal regions derived from 12 climate models (different colors and symbols) following the criteria described in *Wang and Ding* [2006], for land (top) and ocean (bottom) and for different experiments (left symbol in each cluster: 1850 control; middle symbol in each cluster: 4xCO_2; right symbol in each cluster, G1). MMM values are illustrated as black diamonds for each experiment. Areas of monsoonal regions are also shown for the Global Precipitation Climatology Project (GPCP) dataset [*Adler et al.*, 2003], black triangles, and for the Tropical Rainfall Measuring Mission (TRMM) dataset [*Liu et al.*, 2012], black asterisks. See Figure 4 for a definition of regions.

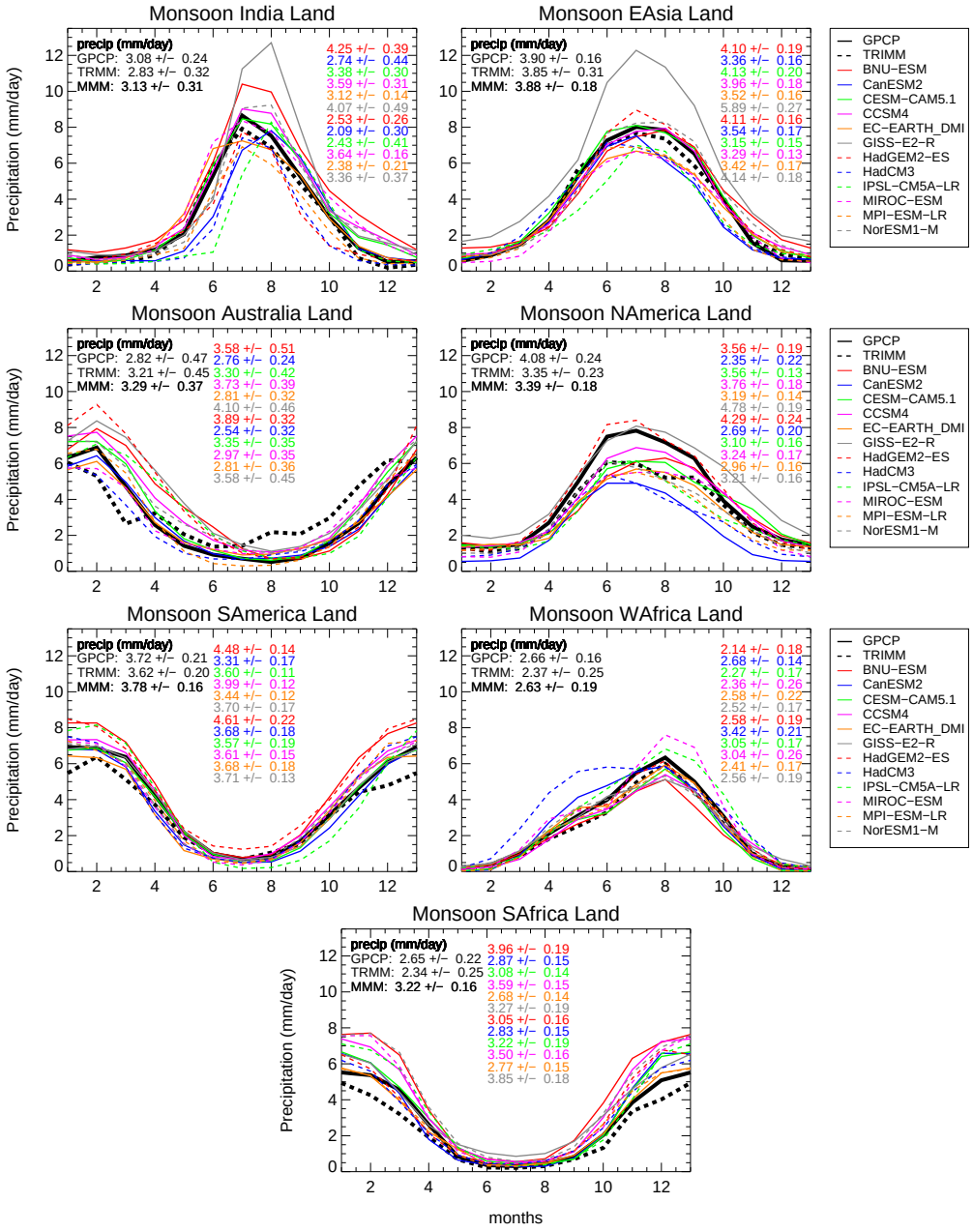

Figure 10. Seasonal cycle of precipitation over monsoonal regions derived from the different GeoMIP model output for the 1850 control simulation (different colors and linestyles) and the GPCP (black solid line) and TRMM dataset (black dashed line). The total precipitation and the standard deviation of annual averages (interannual variability) over each region and each model are listed in each panel in the color and order prescribed in the legend. Values for the MMM total precipitation and the GPCP and TRMM results are shown in black. See Figure 4 for a definition of regions.

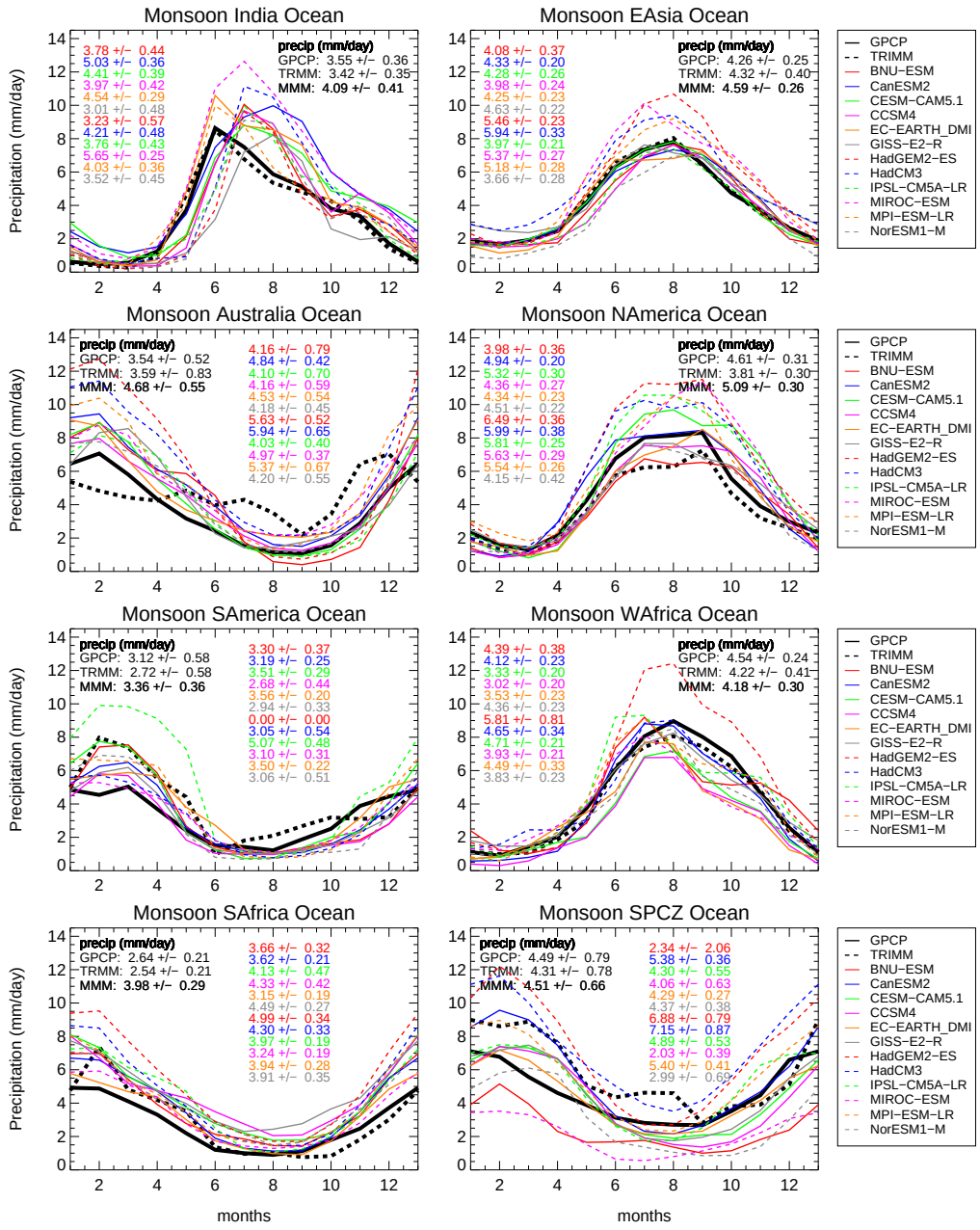

Figure 11. As in Figure 10, for each monsoonal region over ocean.

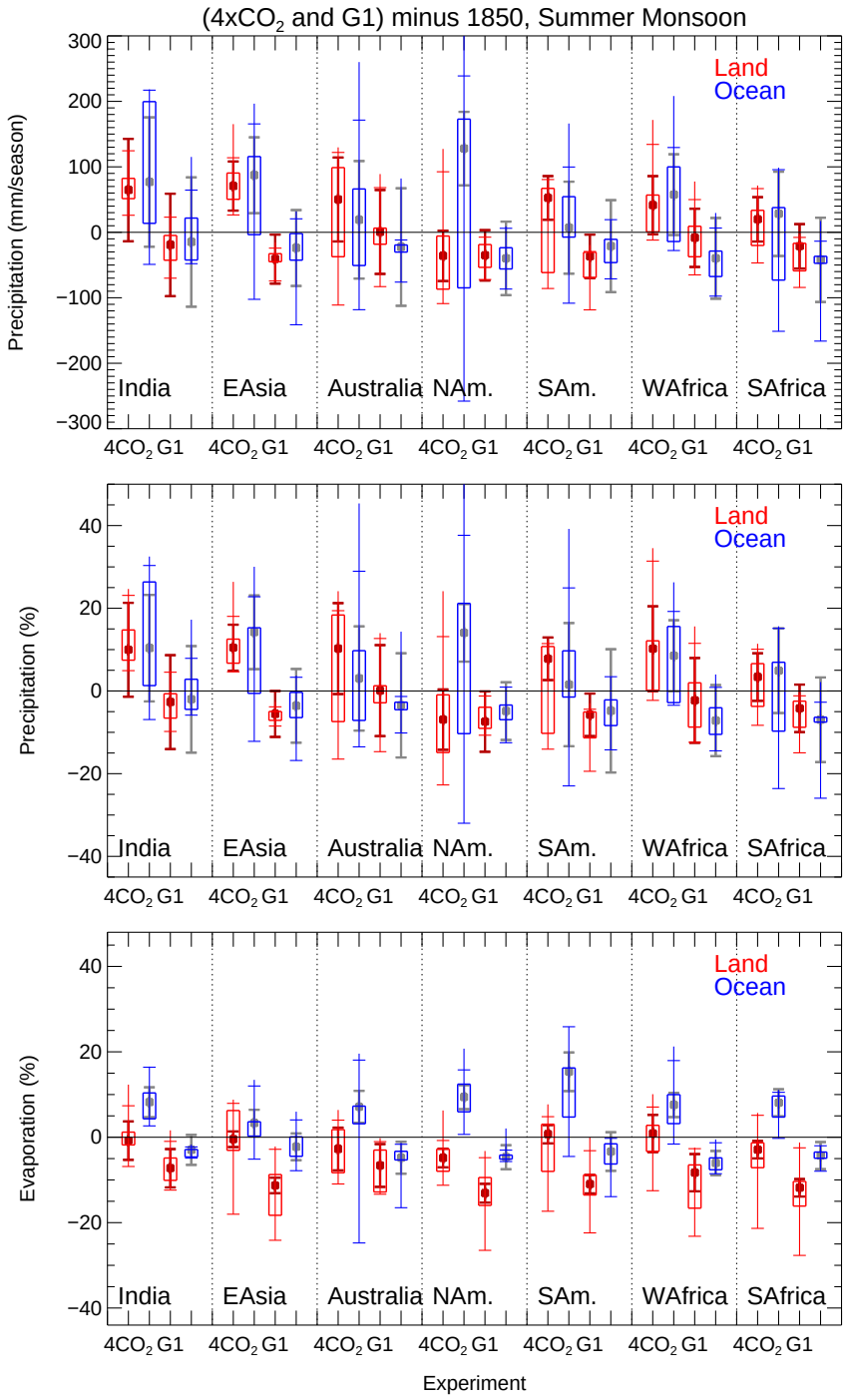

Figure 12. As Figure 6, for each monsoonal region for summer.

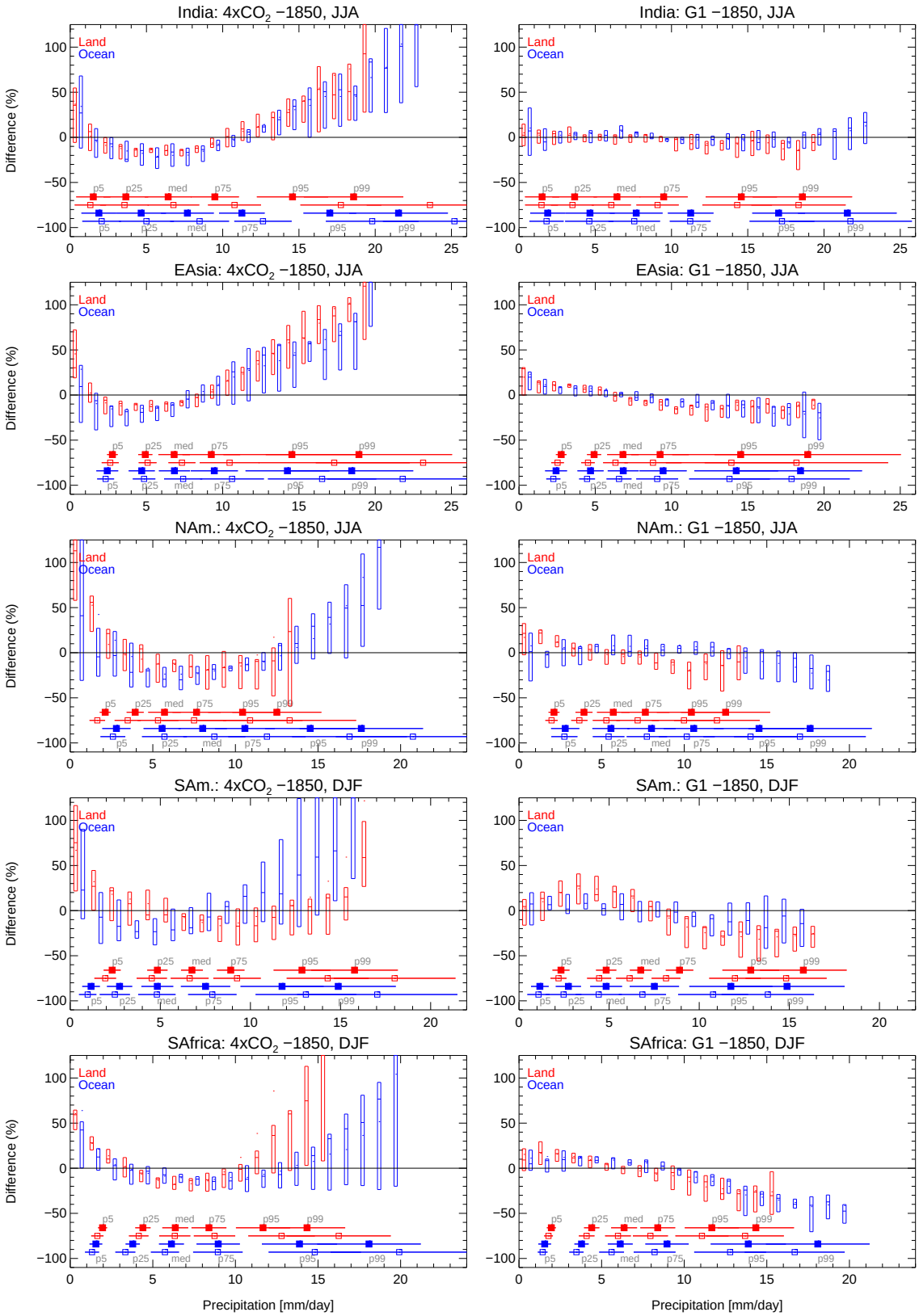

Figure 13. As Figure 7, but for different monsoonal regions and for summer of each region only.

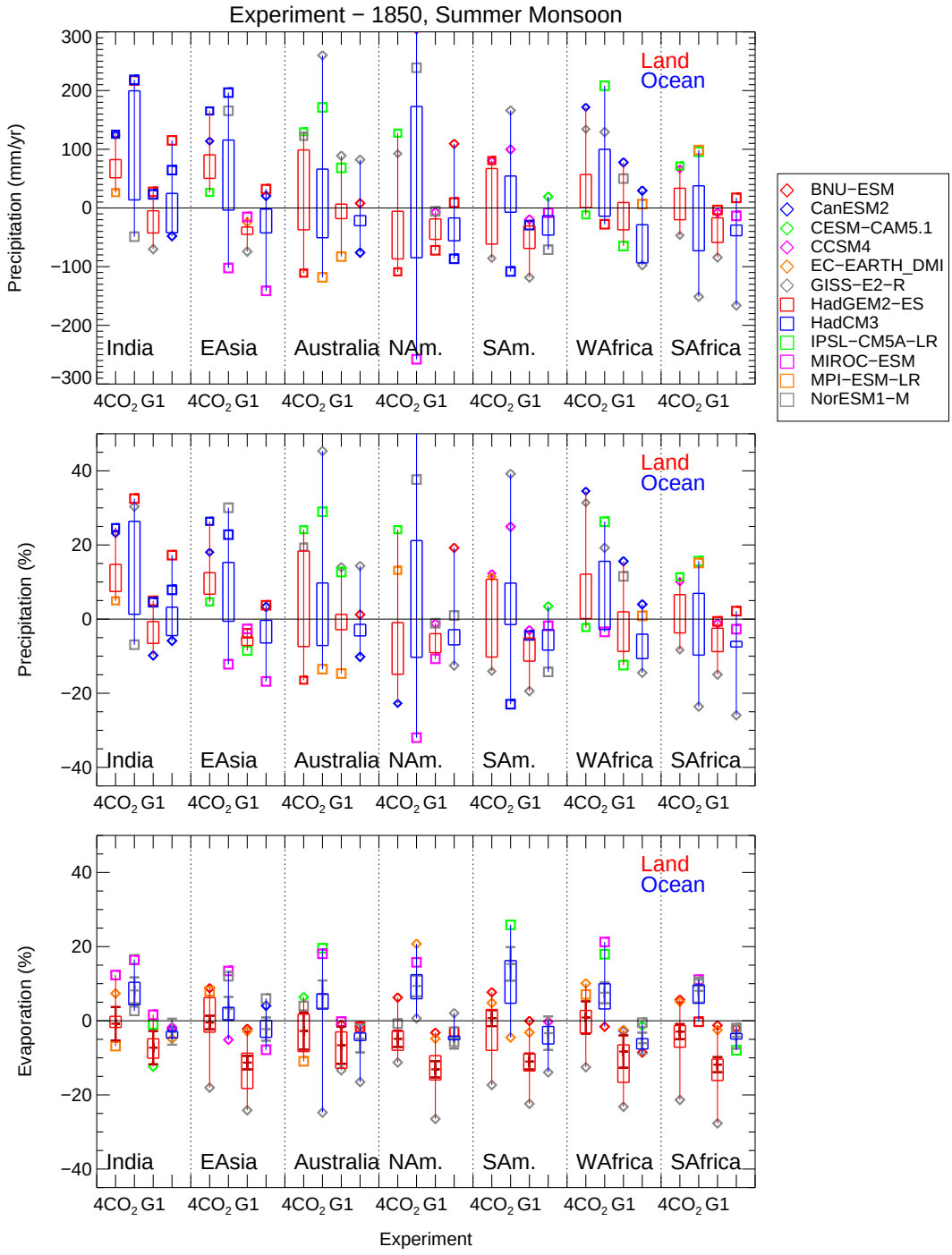

Figure 14. As Figure 12, but with additional information about model results (different symbols) that described value outside the 5th and 95th percentile range of the multi-model distribution.

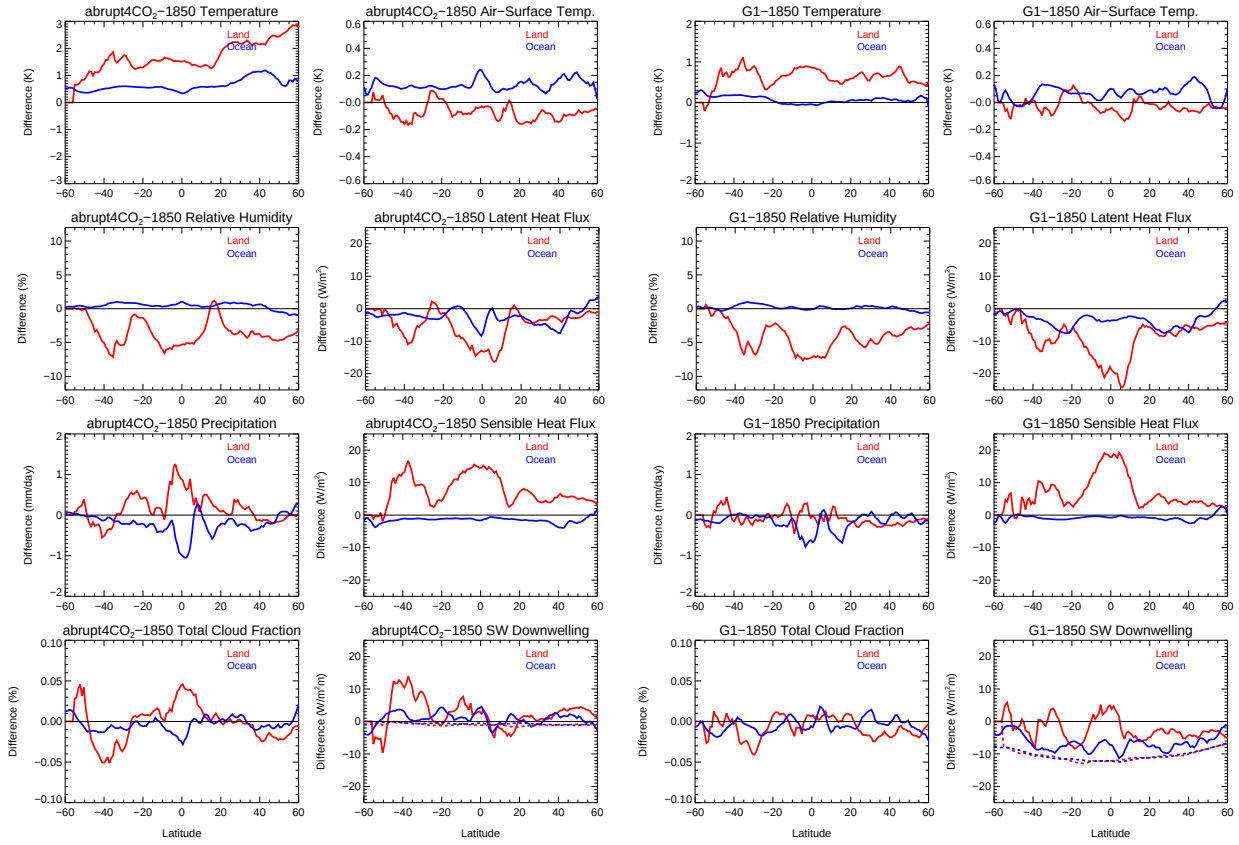

Figure 15. Annually averaged zonal absolute changes of CCSM model results for the first year of the simulation over land (red solid line) and over the ocean (blue solid line) between 4xCO_2 (left) and G1 (right) experiments with regard to 1850 conditions for the following variables: temperatures (first row left); air-to-surface temperature difference (first row right), relative humidity (second row left), latent heat flux (second row right), precipitation (third row left), and sensible heat flux (third row right), cloud fraction (left bottom row), shortwave downwelling with clear sky, dashed, and full sky, solid (right bottom row).

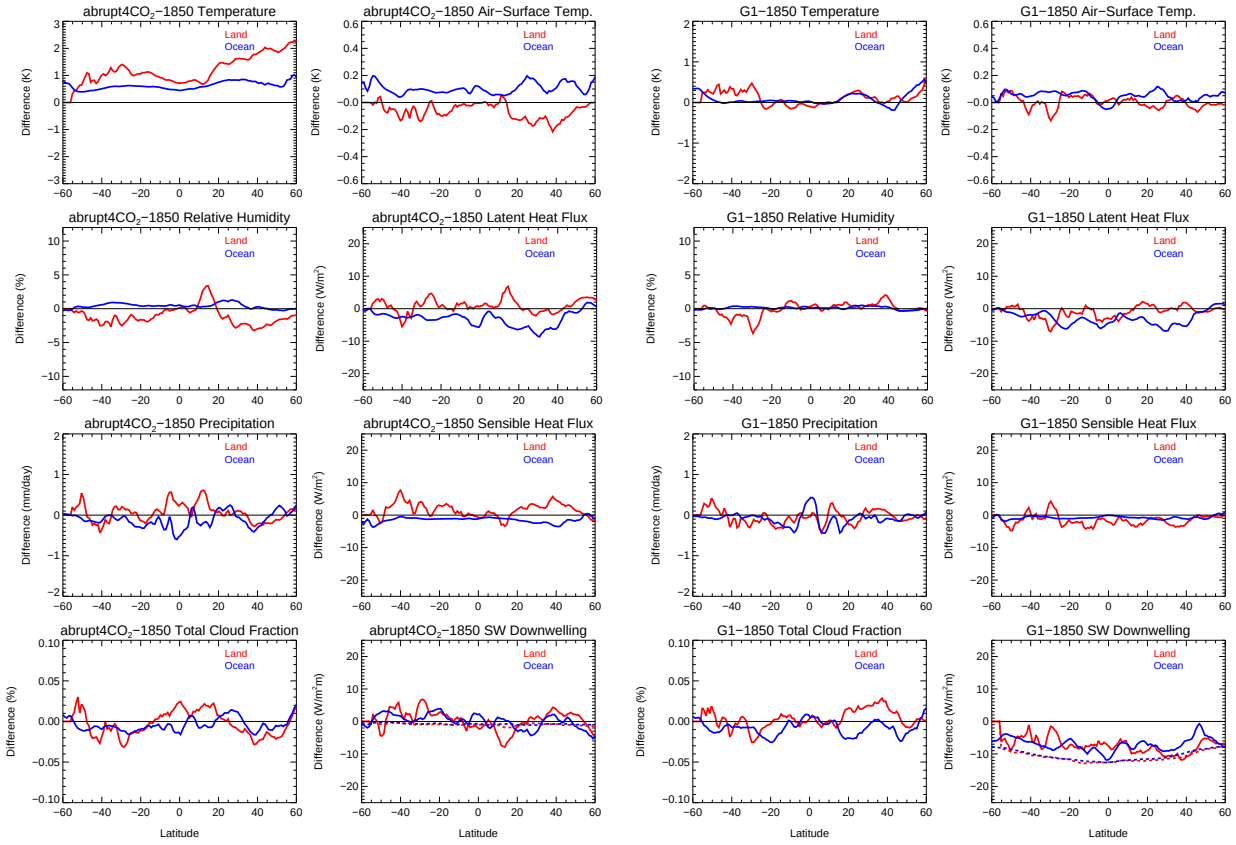

Figure 16. As Figure 15, however, the 4xCO_2 model experiment and G1 do not include any changes in stomatal conductance as a result of the abrupt increase in CO_2 concentrations.